

UNIVERSITÀ DEGLI STUDI DI PADOVA

Dipartimento Di Fisica e Astronomia “Galileo Galilei”

Master Degree in Astrophysics and Cosmology

Master Degree Thesis
Anno Accademico 2021-2022

The Study of the Ionized Gas in NGC 1366 with MUSE Data.

Supervisor: Prof. Alessandro Pizzella
Co-Supervisor: Prof. Lorenzo Morelli

Student: Akshay Kumar
Matricola No.: 1222194

Acknowledgement

I would like to thank all the people who contributed in some way to the work described in this thesis. First and foremost, I thank my supervisor; Professor Alessandro Pizzella and co-supervisor; Professor Lorenzo Morelli, for accepting me to work and for their invaluable patience and feedback.

I am also indebted to my Indian professors: Hum Chand, Ravinder Singh, and Supreet Pal Singh for their support and guidance. They are the reason I am here pursuing my master's in astrophysics and cosmology.

My words cannot express my gratitude to my friend Daxal Mehta for his invaluable support. Without his efforts, my job would have undoubtedly been more difficult. Moreover, Gaurav, Siddesh, Suprio, Andrea, Daniel and many other friends made my time here at the University of Padova a lot more fun.

Furthermore, I am lucky to have met Rashmi Dhamija (particle physicist) during my academic career, and I thank her for her friendship, love, and unyielding support. Finally, I would like to acknowledge friends and family who supported me during my time here. First and foremost, I would like to thank my mother and siblings (Arti and Puneet, Pijush) for their constant love and support. Their belief in me has kept my spirits and motivation high during this process.

Declaration of Authorship

I, Akshay Kumar, declare that this thesis titled, “The study of the ionized gas in NGC 1366 with MUSE data.” and the work presented in it are my own. I confirm that:

- This work was done wholly or mainly while in candidature for a research degree at this University.
- Where any part of this thesis has previously been submitted for a degree or any other qualification at this University or any other institution, this has been clearly stated.
- Where I have consulted the published work of others, this is always clearly attributed.
- Where I have quoted from the work of others, the source is always given. With the exception of such quotations, this thesis is entirely my own work.
- I have acknowledged all main sources of help.
- Where the thesis is based on work done by myself jointly with others, I have made clear exactly what was done by others and what I have contributed myself.

Abstract

The NGC 1366 is a lenticular and bright galaxy at a distance of 17Mpc in the Fornax cluster. It is a challenging case in the panorama of galaxies hosting counter-rotating stellar components. Surprisingly, unlike most of the counter-rotating galaxies, the ionized gas detected in NGC 1366 is not associated with any of its stellar components nor with the main galaxy body, but it has a chaotic distribution and convulsed kinematics with multiple velocity components observed along the minor axis of the galaxy.

The aim of this thesis work is to study the ionized gas in NGC 1366 with the Multi Unit Spectroscopic Explorer (MUSE) data. To study the gas and its characteristics, I have used Python programming and examined the 2D maps of emission line flux, relative velocity and velocity dispersion of the ionized gas and the properties of the gas.

Results: The ionized gas has irregular motion at the center of the galaxy. The emission lines appear to be in an irregular spiral pattern in the whole galaxy. Furthermore, The [NII] and [OIII] are brighter than the H β and H α indicating that there is no star formation in the galaxy. This confirms the peculiarities of NGC 1366 in comparison with the other counter-rotating galaxies.

Contents

1	Introduction	1
1.1	The main ingredients of a galaxy	1
1.2	The Kinematics of Galaxies	2
1.2.1	Optical Determinations Methods	3
1.2.2	Ionized gas study	4
1.3	Kinematic profile	5
1.3.1	Rotational Curves of Spiral Galaxies	5
1.3.2	Elliptical Galaxies	6
1.3.3	Lenticular Galaxies	8
2	Counter Rotating Galaxies	9
2.1	Overview	9
2.2	Observation	11
2.3	Morphological Statistics and Environment	13
2.4	Stellar Populations and Formation scenarios	15
2.5	NGC 1366	18
3	Instrumentation	22
3.1	Very Large Telescope	22
3.2	MUSE Spectrograph	23
3.3	Spectroscopy	26
3.3.1	Long-Slit Spectroscopy	27
3.3.2	Integral Field Spectroscopy	29
4	Results and Discussions	32
4.1	Observation of NGC 1366	32
4.2	Data Reduction and Binning Method	33
4.3	Emission line spectra	35
4.4	Flux Distribution and Kinematical Fields	36
4.5	Ionization Mechanism of Nebular Gas	39
4.6	Discussion and conclusions	41
	Bibliography	42

Chapter 1

Introduction

The mechanisms which lead to the formation and evolution of counter-rotating galaxies are still a topic of debate in the astronomic community. In this thesis, I have studied the gas kinematics of NGC1366,¹ which is a counter-rotating galaxy. I have studied the 2D map of the ionized-gas using the data from the Multi Unit Spectroscopic Explorer (MUSE) on the Very Large Telescope (VLT). Moreover, I have examined the gas properties of NGC 1366 and improve our understanding of galaxy formation and evolution on the smallest scales.

1.1 The main ingredients of a galaxy

A galaxy is a complex system constrained by gravity. According to our current theory, dark matter, whose distribution is significantly wider than that of visible matter and creates a spheroidal halo, dominates the gravitational potential. Ordinary "baryonic matter" is primarily composed of hydrogen and helium and takes the form of stars, diffuse and clumpy gas, dust, planets, and other objects. Baryons are the only particles that emit radiation in the electromagnetic spectrum, whereas dark matter particles are difficult to find since they do not absorb or emit light and only interact with ordinary matter through gravity. Dark matter dominates the mass budget, accounting for about 85% of the total matter content. As a result, in galaxies, the relationship between mass and light is very different. Star formation uses the gaseous component as fuel. The physics of star formation involves a very intricate set of interactions involving gas infall, turbulence, radiative transfer, feedback from star formation, and magnetic fields. Additionally, because dust is frequently found in gas-rich star-forming environments, it serves as a significant tracer of star formation. This element plays a crucial role in the thermodynamics of star formation due to the scattering, absorption, and emission of radiation by dust. The details of the interstellar medium, such as gas temperature,

¹R.A = $03^h 33^m 53.7^s$ and Dec = $-31^\circ 11' 39''$

density, and composition, define the rate at which molecular clouds can form stars. Galaxies with starbursts, or extremely high rates of star formation, are frequently shrouded in dust; the most active regions exhibit strong infrared emission by high temperature dust and are almost opaque to optical radiation, which is the case of submillimetre galaxies (SMGs) or Ultra-Luminous Infrared Galaxies (ULIRGs). Along with these elements, it is important to note that galaxies have supermassive black holes (SMBHs) at their centers. It has a mass ranging from a few million to several billion suns that can regulate the formation of their host galaxy. An Active Galactic Nucleus (AGN), which is extremely bright, forms as gas accretes onto the SMBHs. The energetic output of the AGN in the form of jets may have effects on star formation throughout the entire galaxy, but this is still mysterious.

1.2 The Kinematics of Galaxies

In the middle of the 1970s and earlier, spiral galaxies were the only ones for which progress had been made in measuring the kinematics of external galaxies. Strong emission lines were used for the measurements, either the 21-cm line for atomic hydrogen or the emission lines from ionized gas in star-forming regions throughout the disk. The simple expectation that the rotation in the outer disk should exhibit the Keplerian decline $V \sim R^{-1/2}$ signature was quickly disproved [Van de Hulst et al. \[1957\]](#), but the potential consequences of this realization were not recognized immediately. This eventually resulted in the discovery of dark halos, starting astrophysics' search for dark matter. The kinematics of elliptical galaxies were largely unexplored until the mid-1970s. The first measurements [Bertola and Capaccioli \[1975\]](#), which were based on stellar absorption lines, showed dramatically that the flattening of elliptical galaxies is statistically contrary to rotation. The fact that kinematical tracers similar to those available in spiral galaxies are not systematically present in sufficient amounts in ellipticals leads to a new understanding of their structure.

The kinematical study of galaxies reveals their evolution, and in particular, analysing the gas kinematics of stellar and gaseous components allows us to infer the galaxies' dynamical structure. The advent of wide-field, high resolution integral field spectroscopy (IFS) has revolutionised our understanding of galaxies and its evolution. Instead of obtaining one spectrum of light per galaxy, integral field units (IFUs) allow a galaxy to be viewed in three dimensions (3D), where every spatial pixel (spaxel) across the surface of a galaxy contains a full spectrum of light. The stellar and gas kinematics from each spaxel of IFS data provides a wealth of information that can be used to understand a galaxy's inherent properties and evolution in greater depth. IFU made it possible to get two-dimensional kinematics of gas and stars for the first time, overcoming the limitations associated with one-dimensional velocity

curve interpretation.

1.2.1 Optical Determinations Methods

With the emission lines, we can study the distribution of ionized gases in the galaxies. Whereas absorption lines, which are dominated in the spectrum of a galaxy, are used to get information about the stellar content (the lines come from the atmospheres of the stars). The absorption lines are very difficult to obtain and never extend over the entire disc. However, they are extremely useful, especially for comparing the rotation velocities of stars and gas. By observation It can be seen that from the galaxy's center to a distance of about 20kpc, the velocities of the stars and gas in the disc of spirals does not change by more than the measurement errors (about $30\text{km}\text{s}^{-1}$). With the aid of this fundamental finding, we are better able to extrapolate the dynamics of galaxies from the rotation curves observed for gas. But in the central bulge, the rotational velocity of the stars is only half that of the gas because the stars' rotational velocity there is greatly reduced by the large velocity dispersion of the gas, which is a cold component that traces the mass distribution like test particles. The comparison is difficult, however, because significant noncircular velocities are also present in the stellar and gaseous components (different perturbations, absorptions, bars, and so on); ionized gas rarely orbits the galactic center circularly, and its rotational velocity is frequently lower than that predicted from the visible mass. The rotation curves from the emission lines of ionized gas (mainly $H\alpha$ and [NII]) can be found by the method of long-slit spectroscopy: especially for distant galaxies. It is facile to arrange numerous HII regions along a single slit, normally along the galaxy's major axis. To make the velocity field complete (including noncircular velocities, orientation parameters, and so on), it is important to observe numerous slits spread out across the disc, and the integration time needed may sometimes be long. On the other hand, the Fabry-Perot method of interferometry helps us find large fields at a single time and is being improved further. However, compared to slit spectroscopy, the data reduction is more time-consuming and challenging. The velocity fields of a galaxy from the ionized gas lines are very useful and assist in the HI radio determination. A very high spatial resolution is needed in the central regions, and atomic hydrogen is also often missing from these areas. The HI component is more evenly distributed in the disc regions than it is in the HII regions, but it is pivotal for theories of star formation to take into account all systematic differences between the two components (for instance, those due to the spiral structure).

1.2.2 Ionized gas study

After getting the spectrum of a point in the galaxy, whether it be a point along a slit or a point in a two-dimensional IFU matrix. The ionized gas's kinematics are measured using the procedures listed below:

- Derive the wavelength of the emission and then the redshift.
- Convert redshift into velocity
- By figuring out the precise location of the galaxy's kinematic center and its radial velocity, we can "symmetrize" the rotation curve.
- Adjust the galaxy's velocity for the earth's rotation around the sun and the sun's motion in relation to the cosmic background.
- Find the galaxy's distance from us and the scale (pc/arcsec).
- Deproject the observed quantities (velocities and galactocentric distances) and transform them into physical units.

The redshift z is defined as:

$$z = \frac{\lambda_{observed} - \lambda_{lab}}{\lambda_{lab}} = \frac{\Delta\lambda}{\lambda} = \frac{\lambda_{observed}}{\lambda} - 1 \quad (1.1)$$

To transform the redshift into velocity the following relativistic formula is used which link Z and velocity V of a target:

$$V = c \frac{(z+1)^2 - 1}{(z+1)^2 + 1} \quad (1.2)$$

Where (c = speed of light in the vacuum = 299792.458 km/s) or also,

$$z = \sqrt{\frac{1 + V/c}{1 - V/c}} - 1 \quad (1.3)$$

Often the approximation for $V \ll c$ (or $z \ll 1$) is used. In this case $V=cz$.

To find the scale and distance of a galaxy we used the Hubble law. In the case of small speeds we can use the approximate formula

$$D = \frac{V_{cosmological}}{H_0}; H_0 = 73 \text{ km/s/Mpc} \quad (1.4)$$

For example, a galaxy with $V_{cosmological} = 2000$ km/s is located at a distance of 27.4 Mpc. By measuring V in km/s we get the distance directly in Mpc. With the distance we can derive the spatial scale on the galaxy:

$$\text{scale} = D(\text{pc})/206264.8 = D(\text{Mpc})/.2062648$$

1.3 Kinematic profile

The most used method to determine the kinematics of galaxies is to study its velocity distribution and dispersion through its spectrum. When the source of light is in movement with respect to the observer, it either stretches the wavelength or squeezes it, depending on the direction of source's movements. Conversely, the redshift or blueshift of light tells us whether the source is coming near or going far. Emission lines are the best mappers of a spectrum as comparison to precise laboratory detections easily relay the whole story. Change in the location of emission line tells us the group velocity of a particular cloud while width of the line tells us the individual distribution of velocity within the cloud. Both of which are imperative to study the kinematic profile of the galaxy.

1.3.1 Rotational Curves of Spiral Galaxies

Spiral galaxies are defined by Newtonian rotation, as it follows the equation of Newtonian Mechanics. As such, the velocity V at a certain radius r is given by $V = r\Omega(r)$, which is in the tangential direction. Here, Ω is the differential rotation velocity given determined by the gravitational potential. Usually, perturbations from circular orbits are small, i.e., small pressure gradients. Thus, the rotation equation gives:

$$\frac{V(r)^2}{r} \sim \frac{\partial \Phi}{\partial r} = \frac{GM(r)}{r^2} \quad \text{where} \quad \Phi = -\frac{GM(r)}{r} \quad (1.5)$$

where G and $M(r)$ are gravitational constant and galactic mass, r is galactocentric radius and V is rotational velocity.

Equation 1.5 can be distributed in two regions of the galaxies, leading to two different types of velocity curves. Near the center of the galaxies, mass of the galaxy is a function of radius given by $M(r) = \frac{4}{3}\pi r^3 \rho$ (considering constant density of the galaxy). This gives us a relation $V \propto r$, which is linear. Far from the center, stars and gas are only affected by the mass inside their radius, which makes them feel mass of the galaxy as a constant. As a consequence, 1.5 can be written as $V \propto r^{-1/2}$, which is the Keplerian rotation curve.

Observations of curves follows these expressions to a certain radius after which, they defect. One does not observe the Keplerian fall curve. Instead, the curve becomes flat with a constant V . This can only be satisfied when mass of the galaxy is directly proportional to the radius. There is additional mass outside the galaxy that behaves differently than normal matter, which we term "Dark Matter". For the observed rotational curves, large amounts of Dark Matter must exist in a more or less spherically symmetric halo, reaching far beyond the visible matter. Considering the spherically symmetric distribution, the mass inside the sphere of radius R would be $M(r) \propto r$, so that we obtain a

first rough model of Dark matter density distribution:

$$\rho = (1/4\pi r^2) \frac{dM}{dr} = \frac{V}{4\pi G r^2} \quad (1.6)$$

Equation 1.6 gives $\rho \propto r^{-2}$, for distance outside the visible radius. As we shall see, this model is undoubtedly oversimplified, yet it corresponds to the so-called "nonsingular isothermal" profile which is the most common types of halos:

$$\rho = \frac{\rho_0}{1 + (\frac{r}{r_0})^2} \quad (1.7)$$

with ρ and r_0 are constants.

What are the best components to map the kinematics in spiral galaxy? Molecular gas has the coldest temperature, leading to very small turbulent speed. Stars have elliptical movements and lack strong emission lines. Atomic hydrogen emission is ideal since it is cold (their own movements won't dampen the motion due to gravitation potential, giving us the proper gradient) and it extends beyond what the optical light can capture while maintaining its disk-like shape.

Measuring a given rotation curve, we see the effects of the mass contributed by all the components of the galaxy (gas, bulge, halo). We can divide the velocity equation into its components by writing,

$$V_i^2 = r \frac{\partial \Phi_i}{\partial r}. \quad (1.8)$$

It is easy to determine the mass of disk and bulge given a photometric profile. Similarly, under acceptable assumptions, we can find the gas mass. Then, the above equation becomes

$$V^2 = V_d^2 + V_b^2 + V_g^2 + r \frac{\partial \Phi_h}{\partial r}, \quad (1.9)$$

giving us the potential due to dark matter halo.

1.3.2 Elliptical Galaxies

The radial velocity or line-of-sight velocity distribution (LOSVD) curves are obtained from the spectroscopic study of absorption lines and are typically represented by $V(r)$, in km/s . whereas the velocity dispersion profiles represented by $\sigma(r)$ in km/s are found by measuring the line shifts and linewidths.

The conversion of LOSVD to kinematic profile is dependent on the model we choose, unlike spiral galaxies. $V(r)$ does not relate to local gravitation field at radius, while its meaning is also different from the rotational curve. The general trend we observe for elliptical galaxies is its high velocity dispersion ($\sigma^2 \gg V^2$) and velocity-dispersion profiles have different slopes. In most

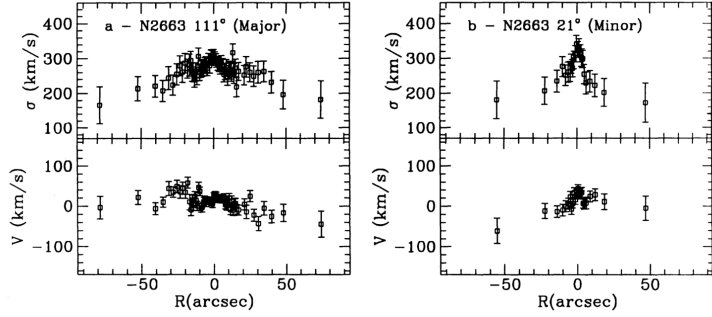


Figure 1.1: Kinematics of the elliptical galaxy NGC 2663 (Carollo and Danziger [1994]) The measurements extend out to $\approx 1.8R_e$.

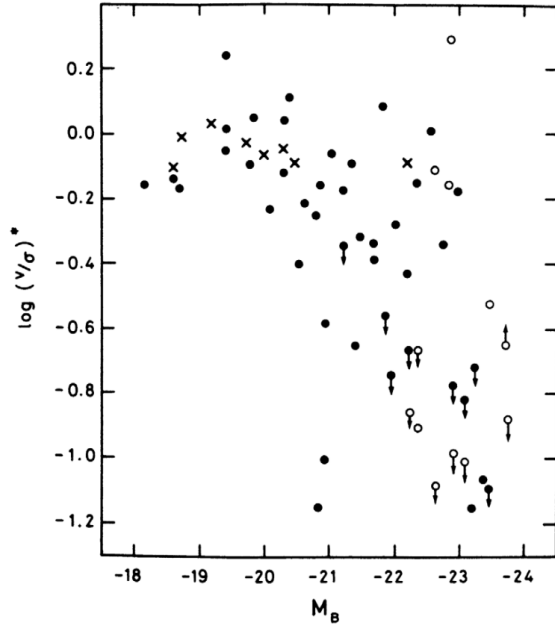


Figure 1.2: The logarithm of the measured systematic velocity to velocity dispersion ratio against the galaxy's absolute magnitude, normalized to the value expected for oblate isotropic rotators. Filled circles are ellipticals, crosses are bulges, open circles are cD and brightest-cluster galaxies de Zeeuw and Franx [1991]

cases, there is no correlation between velocity and dispersion profiles. We also see no effect of rotation on the profiles, leading us to believe that bright, boxy galaxies' shape results from pressure anisotropy.

1.3.3 Lenticular Galaxies

In terms of galaxy morphological classification schemes, lenticular galaxies fall somewhere between elliptical and spiral galaxies. These galaxies are also called as disc galaxies, which have very little ongoing star formation because almost all of their interstellar matter has been consumed or lost. However, they might keep a lot of dust in their disks. As a result, much like elliptical galaxies, they are primarily made up of old stars. Despite their different morphologies, lenticular and elliptical galaxies have similar spectral characteristics and scaling relations. Both galaxies, at least in the region where they are located, can be regarded as early-type galaxies that are passively evolving.

The kinematic characteristics of spiral and elliptical galaxies are both shared by lenticular galaxies. This is because lenticulars have a sizable bulge and are disk-shaped. Because the bulge component is pressure-supported by a central velocity dispersion, it shares characteristics with elliptical galaxies. The rotationally supported disk, however, dominates the kinematics of lenticular galaxies. The stability of the galaxy is said to be caused by the average circular motion of stars in the disk, according to rotational theory. Thus, lenticular galaxies and elliptical galaxies can be distinguished from one another using kinematics. The kinematics of disk galaxies are usually determined by H α or 21-cm emission lines, which are typically not featured in lenticular galaxies due to their general lack of cool gas. There is also a considerable amount of difficulty in deriving accurate rotational velocities for lenticular galaxies. This is a combined issue from lenticulars having unoriented inclination measurements, projection effects in the bulge-disk interface region, and the random motions of stars affecting the true rotational velocities. These effects make kinematic measurements of lenticular galaxies considerably more difficult compared to normal disk galaxies. The kinematic joining between spiral and lenticular galaxies is most clear when analyzing the Tully–Fisher representation for spiral and lenticular samples. If lenticular galaxies are an evolved stage of spiral galaxies, then they should have a similar Tully–Fisher description to spirals but with an offset in the luminosity/absolute magnitude axis.

Chapter 2

Counter Rotating Galaxies

The galaxies in which two components rotate opposite to each other are known as counter-rotating galaxies. In this chapter, I have explained the kinematic and morphological characteristics of lenticulars and spirals galaxies which host counter-rotating components.

2.1 Overview

Generally, the kinematics of a galaxy are determined by the orbits of the stellar body and ionized gas. However, the description may become more complex if several coexisting stellar disks co-rotate or counter-rotate with respect to each other, with respect to the others, or with respect to the gas disk. In particular, galaxies that exhibit counter-rotation fall into the category of multi-spin galaxies, in which two components are observed rotating in directions that are opposite to each other. The detailed discussion on this topic is given by Rubin [1994] explaining the study of galactic kinematics. Galletta [1987] shows the first evidence of counter-rotation in the early-type barred galaxy NGC 4564, where they measured the kinematics of ionized gas and stellar components rotating in opposite directions around the same rotation axis. At the same time, similar results from other studies were published like Bertola and Bettoni [1988], Bettoni [1984] in NGC 5898 elliptical. With more available data, numerous galaxies are found hosting counter-rotating components. Still, a lot of interesting results are coming out about these galaxies. The *apparent* and *intrinsic* are two kinds of counter-rotating components that occur in galaxies. In the former case, the line of sight is located between the two kinematically separated components as they rotate about skewed rotation axes, causing the vectors of angular momentum to be projected antiparallel onto the sky plane. In the latter type, the two kinematically detached components rotate counterclockwise around the same rotation axis, and as a result, their angular momentum vectors are antiparallel.

According to the galactic components impacted by the counter-rotation, the phenomenon can manifest itself in three different ways.

- *Gas counter-rotation against stars (gaseous counter-rotation)*: If the gaseous disc rotates against the stellar body of the galaxy, as in the case of NGC 4546, galaxy SB0/SBa where ionized, molecular, and atomic gas ($\approx 10^8 M_\odot$) counter-rotate with respect to the stars (Galletta [1987], which historically was the first article in which the phenomenon was highlighted).
- *Counter-rotation of gas against gas*: In this system, two gaseous disks counter-rotate with respect to each other. For instance, the gaseous content ($\approx 10^5 M_\odot$) in S0 NGC 7332 Plana and Boulesteix [1996], Fisher et al. [1994] shows non-circular motions, implying that equilibrium has not been reached.
- *Counter-rotation of stars against stars (stellar counter-rotation)*: In this phenomenon, two stellar components counter-rotate. The E7/S0 NGC 4550 consists of two counter-rotating stellar disks, one of which rotates alongside the gaseous disk see Rubin et al. [1992]; Johnston et al. [2013]; Coccato et al. [2013] others a few examples are NGC 524: Katkov et al. [2011], NGC 2950; Corsini et al. [2003b]; Maciejewski [2006]. This episode is also observed in the NGC 1366 (see section 2.5) by Morelli et al. [2017] and examine the kinematics of the ionized gas in this galaxy is my current thesis work.

The counter-rotation is observed in the different regions of disk galaxies. The Sa NGC 3593 (see Figure 2.1) has counter-rotation in the inner region of the galaxy, and it has a main stellar disk with $\sim 80\%$ of the stars ($1.2 \times 10^{10} M_\odot$) and a secondary counter-rotating disk Bertola et al. [1996]; Coccato et al. [2013], which corotates with the disk of ionized and molecular gas and dominates the kinematics in the inner kpc, according to García-Burillo et al. [2000]. The Sab NGC 4286 (M64) contains stellar counter-rotation in the outer part of the galaxy Braun et al. [1992]; Walterbos et al. [1994]. They have the same masses and are both coplanar to the stellar disk. Most of the stars corotate with the inner gas while only $\lesssim 5\%$ corotate with the outer gas Rix et al. [1995]. The gaseous component of the Sa NGC 3626 is the first spiral galaxy where counter-rotation of the gaseous component ($\approx 10^9 M_\odot$) with respect to the stars was observed at all radii Ciri et al. [1995]; García-Burillo et al. [1998]; Haynes et al. [2000].

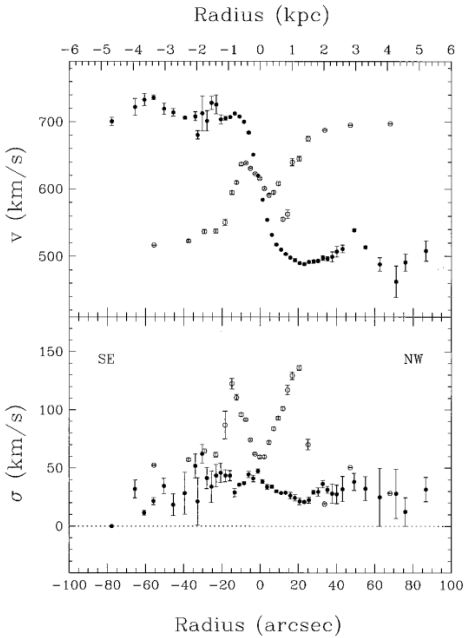


Figure 2.1: The kinematics of NGC 3593: radial velocity profiles (top) and velocity dispersion (bottom) profiles for counter-rotation; empty circles represent the stars, the circles are filled with ionized gas.

2.2 Observation

Generally the observation of counter-rotation of gaseous components in galaxies is very easy. One can tell by examining the position velocity diagrams (as shown in Figure 2.2) or scrutinizing at the contrary direction of the stellar absorption and ionized gas emission lines in two-dimensional optical spectrum (as shown Figure 2.3). The standard methods are used to calculate the kinematics of stars and gas, which allows measuring variations of the rotational velocities in a few km/s. However, exploitation of a counter-rotatation of stellar and gaseous component is very arduous job. As the counter-rotating stellar kinematics of two components are determined by the alike absorption lines. and thus thorough data analysis is necessary. If the two components have the same photometric properties, we can observe the x-shaped absorption lines. However, The presence of two counter-rotating components is indicated by the presence of a dualmode line-of-sight velocity distribution (LOSVD). The instrumentation used for the spectroscopic observation and the properties of the galaxies affect the measurement of LOSVD bimodality. Through examining artificial spectra with various percentages of counter-rotating stars, [Kuijken et al. \[1996\]](#) & [Pizzella et al. \[2004\]](#) gave a maximum limit of 10% for the retrograde stars that can be seen in spectra with long slits and medium resolution ($\sigma \simeq 50 Kms^{-1}$) having a spatial resolution of $FWHM \approx 1''$ with a signal-to-noise ratio, $S/N \geq 30 \text{\AA}^{-1}$. [Coccato et al. \[2013\]](#), have shown the

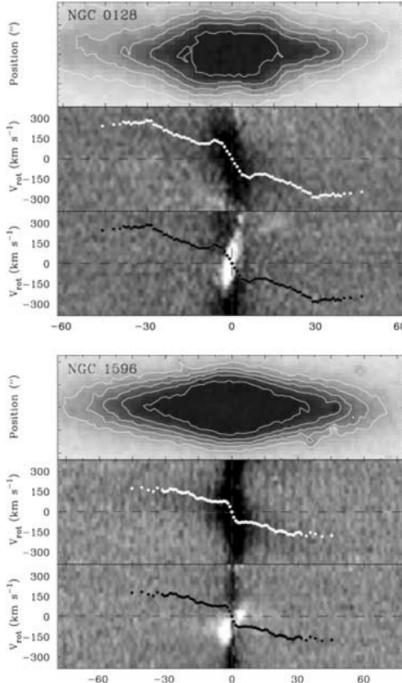


Figure 2.2: Shows the Kinematics of stellar and ionized gas of NGC 128 (upper) and NGC 1596 (lower). Each image describe the grey-scale of the galaxy with contours from the DSS, where white dots represents the plotting of stellar rotation curve on a stellar absorption line. Similarly, the black dots depict the information of stellar rotation curve and emission line. ([Bureau and Chung \[2006\]](#))

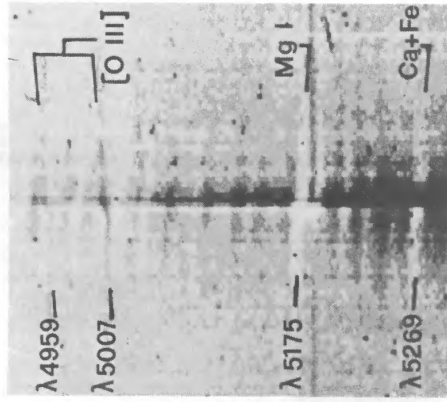


Figure 2.3: Opposite orientation of the emission lines of the ionized gas [OIII] and those in absorption related to the stellar body in a two-dimensional optical spectrum along the major axis of the galaxy NGC 4546, host of gaseous counter-rotation. ([Galletta \[1987\]](#))

same results for the integral-field spectra. The Gauss-Hermite expansion ([Van Der Marel and Franx \[1993\]](#)) does a poor job of recreating a galaxy's LOSVD if it has secondary kinematic components ([Katkov et al. \[2013\]](#); [Fabricius et al. \[2012\]](#)). Additionally, the LOSVD's variation and noise characteristics can simulate what might be seen as a counter-rotating component. Therefore, it is necessary to carried out with care when recovering and decomposing parametric LOSVDs. In fact, [Bottema \[1999\]](#) demonstrated that the counter-rotating bulge of the Sb NGC 7331 discovered by [Prada et al. \[1996\]](#) was a relic of the technique used to measure the stellar kinematics. Evidence suggests that two counter-rotating disks exist when there are two askew and uniform apexes in the stellar velocity and stellar velocity dispersion and zero velocity rotation measured along the galaxy's major axis. Also, If we observe two counter-rotating components along the radial range, their LOSVDs are unresolved, and their luminosity are almost equal. [Krajnović et al. \[2011\]](#) discovered 11 galaxies, such as NGC 4550, in the restricted volume sample of 260 nearby early-type galaxies collected through the ATLAS-3D project. To understand the percentage of their counter-rotating stars, they are intriguing candidates for further study.

2.3 Morphological Statistics and Environment

Most of the galaxies that host counter-rotating components have undisturbed morphologies. There is no proof of recent connection with any similar size body, satellites or any events. In fact their environment statistically does not seem to differ from that of typical galaxies, as explain by [Bettoni et al. \[2001\]](#). They examined extensively environments of 43 companion galaxies having no counter-rotation and 49 with the counter-rotation. They study the quantity, size and dispersion of bright companions (inside the redshift difference <600 Km/s and radius <0.6 Mpc) and faint satellites (of limiting magnitude <21.5). These results impose limits on the origin of counter-rotation since the formation activity must preserve the host galaxies' current morphology and their surrounding density. As a result, retrogressive gas accretion must be a straightforward process. Major mergers should only occur early in the host galaxy's existence. Whilst minor mergers could have happened more recently, the remnants of the major events, such as tidal tails and collisional debris are typically fleeting and inconspicuous objects. Their typical remaining ages are between a few Myr and a few hundred Gyr with the surface brightness less than 27 B-mag $arcsec^{-2}$ while getting old and 25 B-mag $arcsec^{-2}$ when they are young. A profound optical survey is necessary for the diagnosis of these minute structures, However, the period and mechanism of the second event may be constrained by comparing kinematic and morphology with the numerical simulations (e.g., [Duc et al. \[2011\]](#); [Corsini et al. \[2002\]](#)).

When it comes to the morphology of the host galaxy, no counter-rotating

components are found in late-type spiral galaxies. The galaxies NGC 3593, NGC 3626, and NGC 4138 fall into the category of early-type spirals (S0/a–Sa) with smooth arms that contain counter-rotating gaseous and stellar disks. Their dust lanes either completely define or predominate their spiral pattern. In fact, they are included in the same chapter of The Carnegie Atlas of Galaxies([Sandage and Bedke \[1994\]](#)). High-resolution N-body simulations of multi-armed spiral features have revealed the suppression of arms in counter-rotating spirals. There were kinematically decoupled gas components found in early S0/a and Sa spirals, but there were no new instances of counter rotation ([Corsini et al. \[2003a\]](#)). The N-body simulations ([Comins et al. \[1997\]](#); [Lovelace et al. \[1997\]](#)) have shown that galaxies with a significant percentage of counter-rotating stars may have a stationary and persisting one-arm leading spiral wave. Previous simulations have failed to detect such a wave due to high inclination and a lack of kinematic data for low inclined spirals.

The counter-rotating gaseous components in the 17/53 galaxies were discovered by looking through the archive data for S0 galaxies ([Pizzella et al. \[2004\]](#)). The kinematics of stellar and ionized gas were measured, and the study was conducted along their major axis. The final percentage of $32\%^{+19}_{-11}$ is nearly in line with previous research (see [Bertola et al. \[1992\]](#), 35% percent and [Kannappan and Fabricant \[2001\]](#), $24\%^{+8}_{-6}$). These results support a hypothesis that the acquisition processes in S0 galaxies are ubiquitous [Bertola et al. \[1992\]](#), similar to ellipticals [Bertola and Bettoni \[1988\]](#), and not restricted to some peculiar objects. With the observation of radio and integral field spectroscopy, [Davis et al. \[2011\]](#) got the same results, which supported the same scenario. They discovered that gas is kinematically out of alignment with the stars in their sample 40/111 ($36 \pm 5\%$) of fast-rotating early-type galaxies. Additionally, the kinematics of molecular, atomic and ionized gas observed in these galaxies were aligned even when their alignment with the stars is off. This highlights the significance of external acquisition and suggests that the source of all these interstellar medium phases is similar. Considering the common occurrence of counter-rotating gas in S0 galaxies, [Kuijken et al. \[1996\]](#) measured that only 10 percent of S0 galaxies contain a remarkable fraction (>5 percent) of counter-rotating stars. Whereas, with the data of 50 S0/a-Scd galaxies, [Pizzella et al. \[2004\]](#) examined the occurrence of counter-rotation in spiral galaxies. For each of the galaxies, the kinematics of the stellar and ionized gas were measured along the major axes using the same analysis technique, spectral resolution, and spatial resolution. It is found that in these sample of counter-rotating galaxies 12 and 8 percent contains counter-rotating gaseous and stellar disk. [Kannappan and Fabricant \[2001\]](#) set the proportion of spirals containing counter-rotating gas to a maximum of 8% by examining at a sample of 38 Sa-Sbc galaxies.

2.4 Stellar Populations and Formation scenarios

To understand the competing theories for the origin of the counter-rotation in disk galaxies, it is expected that the retrograde and prograde have different characteristics like their age difference and α -enhancement. The accumulated gas followed by star formation always predicts a younger age for the counter-rotating components. However, the counter-rotating component created by the retrograde capture of stars through minor or major mergers can be either younger or older than the pre-existing stellar disk. Additionally, two counter-rotating members can have various alpha-enhancements and metallicities owing to the external source. On the other hand, the formation of massive counter-rotating stellar disks as a result of bar dissolution implies that both the retrograde and prograde components could have the same age, mass, and chemical composition. A spectroscopic disintegration that segregates the proportionate patronage of each component to the observed galaxy spectrum is necessary to separate the stellar populations of the counter-rotating stellar components from one another. NGC 5719, NGC 4550 and NGC 3593 which are studied for the counter-rotating stellar disk by [Coccato et al. \[2011\]](#),[Coccato et al. \[2013\]](#); [Johnston et al. \[2013\]](#) and [Coccato et al. \[2013\]](#) respectively. They found that the counter-rotating stellar disk is younger, less massive, quite metal poor, and more α -enhanced and rotates the same way that the ionized gas is moving. These results support the premise that secondary stellar components were formed from gas coalesced on retrograde orbits from the surroundings, allowing a rapid star formation in place from the outside in. [Figure 2.4](#) depicts the splendid continuous face on interaction of the NGC 5179 Sab and NGC 5713 Sbc spiral galaxies ([Vergani et al. \[2007\]](#)). This interaction is reproduced by the tidal span of HI (neutral hydrogen), which supplies the oppositely rotating gaseous and stellar components. Moreover, NGC 5719 (see [Figure 2.5](#)) is the first interacting disk galaxy where counter-rotation has been found. Its counter-rotating and main stellar components have an age of 2 to 13.5 Gyr and 0.7 to 2.0 Gyr respectively. The metallicity range is from supersolar ($[Z/H] \simeq 0.3$ dex) in the center to the subsolar ($[Z/H] \simeq -1.0$ dex) in the vicinity.

[Figure 2.6](#) shows the star formation history by the timescale of 2 Gyr and α -enhancement of the counter-rotating component. However, in the case of NGC 4550 and NGC 3593, the formation via a major galaxy merger cannot be completely ruled out, and these galaxies are relatively undisturbed and isolated ([Coccato et al. \[2011\]](#); [Coccato et al. \[2013\]](#)). More data required to determine whether merger or accretion is the most effective way to assemble the counter-rotating spirals.

The formation of counter rotating galaxies is still a great mystery to us. Continuous research on these galaxies is needed to understand the various

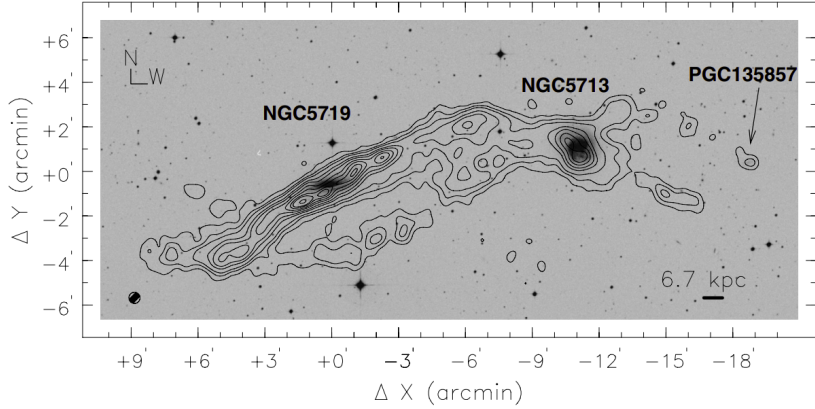


Figure 2.4: The contour map for the interaction of NGC 5179/13, which examine through neutral hydrogen (HI) column density. The minimum contour level is $7.0 \times 10^{19} \text{ atoms cm}^{-2}$ and the growth is $2.4 \times 10^{20} \text{ atoms cm}^{-2}$. (Vergani et al. [2007])

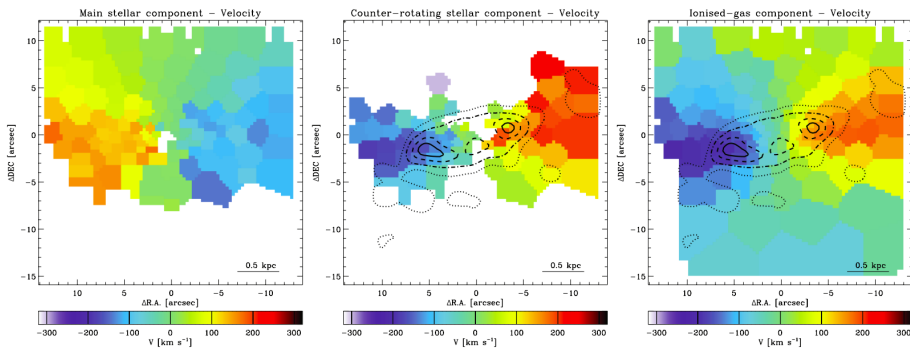


Figure 2.5: Shows the 2-D map of the velocity field for ionized gas and stellar components in NGC 5179. (Coccato et al. [2011])

phenomena like merging and accretion events in the surroundings of counter-rotating galaxies and the vast measurement of the stellar populations of their retrograde and prograde components. By numerical simulations, merging with a gas-rich dwarf companion (Thakar et al. [1997]) and episodic or prolonged accretion of gas from the environment (Thakar and Ryden [1998]) are both potential mechanisms for the retrograde acquisition of small amounts of external gas. They only produce counter-rotating gaseous disks in S0 galaxies because the acquired gas is swept away by the pre-existing gas in spiral galaxies. Due to the gas-poor nature of S0 galaxies, the establishment of counter-rotating gas disks is preferred in S0 galaxies. Whereas the spiral disks contain abundant gas that rotates in unison with the stellar components (Bettoni et al. [2003]). If the system obtains the extra gas in its retrograde orbits, then the clouds of gas from the newly added retrograde and antecedent prograde struc-

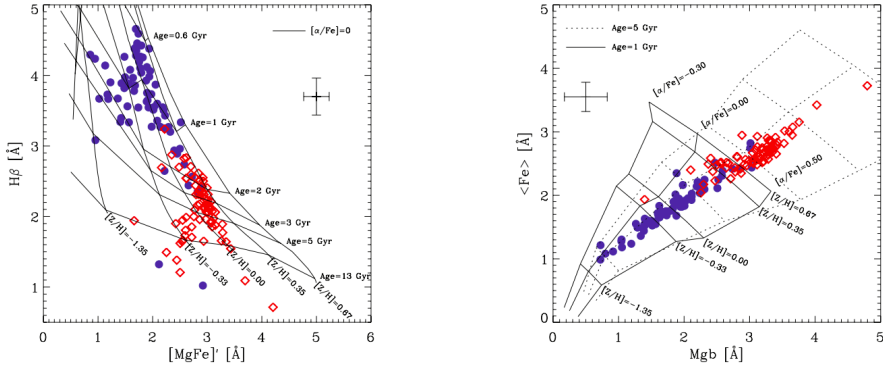


Figure 2.6: The line strengths of the Lick indices measure as $[MgFe]$ versus $\langle Fe \rangle$ (right side) and $H\beta$ versus $Mg b$ (Left side). The blue and red diamonds are for the counter-rotating and main stellar components. (Coccato et al. [2011])

tures collide. As a result end up losing their centrifugal aid and coalescing toward the galactic center. To observe the counter-rotating gaseous disk, it is important to see that the mass of the antecedent is less than the newly supplied gas in the system (Lovelace and Chou [1996]). The reason why there is a small observation of gaseous counter-rotation disks in spirals other than S0 is that the final product of star formation in the counter-rotating gas component is a counter-rotating stellar disk (Pizzella et al. [2004]). Additionally, this explains why the mass of the counter-rotating gas is typically less than that of the stellar counter-rotating components in most S0 galaxies (Kuijken et al. [1996]). Pizzella et al. [2004] examined that both counter-rotating stellar and gaseous disks of spirals, which are frequently seen, are caused by the retrograde acquisition of significant gas. In this model, star formation in a gaseous disk that is rotating counterclockwise leads to stellar counter-rotation. Algorry et al. [2014] has discussed the cosmological simulations of material accreted from two different filamentary structures lead to the formation of two counter-rotating stellar disks.

Generally, the mergers of disk galaxies with similar masses are excluded because they frequently result in ellipticals. However, most of the mergings are successful in creating a strikingly axisymmetric disk that contains two similarly massive and sized counter rotating stellar components for a limited range of initial conditions (see Puerari and Pfenniger [2001]). Additionally, the observation in NGC 4550 demonstrates that the two counter-rotating primogenitors coalesce more rapidly and heat up the prograde stellar disk more rapidly than the retrograde stellar disk, causing the gas to align with the prograde stellar disk and the total angular momentum (Crocker et al. [2009]).

After examining NGC 4550, a different approach with potential external origins has been put forth (Evans and Collett [1994]), which includes the dis-

sipation of a bar or a triaxial stellar halo. For this system, the moving stars in the box orbits are able to leave the restricting azimuthal potential well and transition to tube orbits. For non-rotating disks, both clockwise and counterclockwise azimuthal motions have the same number of box orbits. Therefore, box-orbit stars are dispersed on both clockwise and counterclockwise streaming tube orbits, which leads to the formation of two indistinguishable counter-rotating stellar disks.

Taking into account the barred galaxies' nearly circular retrograde orbits, the counter-rotating stellar components can develop as a result of internal dynamical processes in barred galaxies (Wozniak and Pfenniger [1997];Bettoni [1989];Bettoni and Galletta [1997]). However, gas accreted in this category of retrograde orbits eventually forms new stellar formations. These counter-rotating materials could result in the development of a secondary bar rotating counterclockwise to the primary one (Sellwood and Merritt [1994]). The origin of secondary bars that rotate against the direction of the primary bar can be determined through observation. In fact, the theory that gas instabilities flowing along the main bar cause secondary bars to form is the one that is generally accepted as to how secondary bars form (Shlosman et al. [1989]). A prograde disk, however, is unlikely to support a retrograde bar. The two counter-rotating recursive bars that were created in two overlapping, counter-rotating stellar disks appear to be stable and long-lasting systems, according to numerical simulations (Friedli [1996]). This suggests that secondary bars, like those seen in the centers of several disk galaxies, may develop from inner stellar disks (Pizzella et al. [2002];Ledo et al. [2010]). So far, only elliptical galaxies have counter-rotating nuclear disks (Morelli et al. [2004]).

2.5 NGC 1366

NGC 1366 is a lenticular and bright galaxy at a distance of 17Mpc in the Fornax cluster. According to the classification of De Vaucouleurs (RC3), It has $S0_1(7)/E7$ classification because of its highly inclined thin disk. Despite being a member of the LGG 96 group Garcia et al. [1993], this galaxy exhibits an undisturbed morphology and lacks any nearby bright companions. For observing this galaxy, The total absolute B magnitude is $M_{B_T}^0 = -18.30$ mag and at a surface brightness level of $\mu_B = 25\text{mag arcsec}^{-2}$ the apparent isophotal diameter are 2.1×0.9 arcmin corresponding to 10.4×4.5 kpc. Morelli et al. [2008] discovered that an exponential disk and a Sérsic bulge with a bulge-to-total luminosity ratio of $B/T=0.2$ are good fits for the object's surface-brightness distribution. Moreover, they found a stellar component that is kinematically decoupled and is younger than the host bulge and likely formed from enriched material that was acquired through interaction or minor merging.

Furthermore, NGC 1366 galaxy is studied by Morelli et al. [2017] and discovered that it consists of two counter-rotating stellar components. Ta-

ble 2.1 shows the relative luminosity and properties of the two counter and co-rotating stellar components based on the averaged line-strength indices on the two galaxy sides. Figure 2.7 shows the properties of the stellar population of both components from the line-strength indices averaged on the two galaxy sides, while Table 2.2 shows the errors on the equivalent widths of the line line-strength indices. From the Table 2.1, we can see that compared to the co-rotating stellar component, the counter-rotating stellar component is younger, has almost the same metallicity, and is less α -enhanced. The age and metallicity of counter-rotate are 2.6 Gyr and $[Z/H]=-0.18$ dex, and of co-rotate are 5.6 Gyr and $[Z/H]=-0.16$ dex.

Components	L/L_T	Age [Gyr]	$[Z/H]$ [dex]	α/Fe [dex]
Counter rotating	0.55	2.6 ± 0.5	-0.16 ± 0.11	-0.07 ± 0.08
Corotating	0.45	5.6 ± 2.7	-0.18 ± 0.16	0.08 ± 0.13

Table 2.1: Shows the characteristics of counter-rotating and corotating stellar components of NGC 1366.(Table taken from Morelli et al. [2017])

r ["]	$H\beta[\text{\AA}]$	$Mg_b[\text{\AA}]$	$Fe_{5270}[\text{\AA}]$	$Fe_{5335}[\text{\AA}]$
Counter-rotating components)				
-20.9	2.40 ± 0.32	2.57 ± 0.32	2.70 ± 0.38	2.54 ± 0.35
-12.6	2.85 ± 0.26	2.22 ± 0.26	2.42 ± 0.27	2.32 ± 0.27
11.4	2.35 ± 0.22	2.44 ± 0.21	2.35 ± 0.25	2.23 ± 0.29
19.9	2.59 ± 0.26	1.87 ± 0.33	1.84 ± 0.39	1.83 ± 0.38
Corotating components				
-20.9	1.72 ± 0.71	2.32 ± 0.79	2.11 ± 0.89	1.32 ± 0.80
-12.6	1.43 ± 0.48	2.51 ± 0.48	2.16 ± 0.47	1.392 ± 0.49
11.4	2.27 ± 0.36	3.03 ± 0.33	2.94 ± 0.39	2.52 ± 0.44
19.9	2.57 ± 0.51	2.76 ± 0.60	2.47 ± 0.68	2.02 ± 0.68

Table 2.2: Shows the line-strength indices of the counter-rotating and corotating stellar components of NGC.(Table taken from Morelli et al. [2017])

Moreover, the stellar kinematics of NGC 1366 were studied along the minor and major axis. They couldn't detect any kinematic evidence of stellar decoupling along the minor axis of NGC 1366 as shown in Figure 2.8. The velocity curve is defined by $|v| \simeq 0$ km/s at all radii, demonstrating that the galaxy's photometric and kinematic minor axes are in alignment. The velocity dispersion profile is smoothly decreasing radially from $\sigma \simeq 150$ km/s in the center to $\simeq 60$ km/s at the last measured radius ($r \simeq 14''$). Figure Figure 2.9, shows the anomalous stellar kinematics along the galaxy's major axis. The spectral absorption lines for $|r| \geq 11''$ clearly show a double peak that is caused by the velocity difference of the two counter-rotating components. For the innermost radius of $|r| \leq 11''$, the velocity curve is symmetric

around the center. Furthermore, it is depicted by a steep ascent with a peak of $|v| \simeq 50$ km/s at $|v| \simeq 2''$ and decreasing farther out to $|v| \simeq 0$ km/s at $6 \lesssim |r| \lesssim 11''$. The counter-rotating and co-rotating components are related to the velocities measured at large positive and negative radii, respectively. The velocity dispersion is maximum at $\simeq 150$ km/s and decreases externally. It increased again at $\simeq 140$ km/s at $|r| \simeq 9''$ and decreases to a value of $\simeq 100$ km/s at $|r| \simeq 25''$. Two counter-rotating components are suggested by the stellar component's velocity dispersion, which has zero velocity and two off-centered, symmetric peaks measured along the galaxy's major axis. By comparing the ionized-gas and stellar velocity curve, It is clear that the gas is disturbed and not connected to either of the two counter-rotating components. Additionally, this galaxy exhibits an undisturbed morphology and shows no evidence of recent interactions with small satellites or companion galaxies of a similar size, nor does it show any signs of dissolved bar remnants. The ionized gas found in this galaxy is not connected to either the main galaxy body or the younger counter-rotating stellar component. However, Its distribution is disorganized, and its convulsed kinematics, which are seen along the galaxy's minor axis, have multiple velocity components. As a result, theoretical models find this galaxy to be very mysterious. The goal of this thesis is to examine the kinematics of the ionized gas in the galaxy.

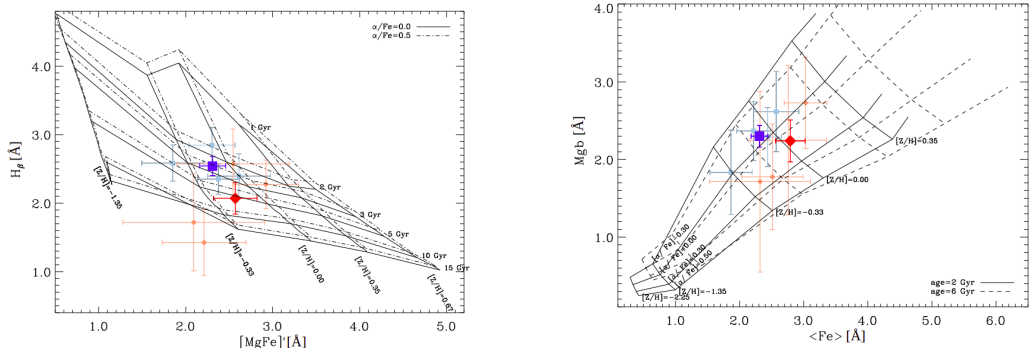


Figure 2.7: Line strength indices for the Values of $H\beta$ and $[MgFe]$ and $\langle Fe \rangle$ and Mg_b (right side) for the counter-rotating stellar component (small blue squares) and corotating (small red diamonds) measured along the major axis of NGC 1366.

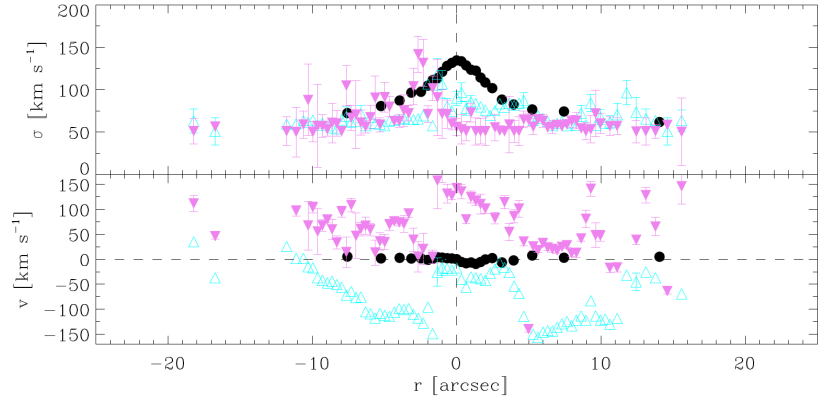


Figure 2.8: Shows the radial velocity profile (lower panel) and line-of-sight velocity dispersion (top panel) for the total stellar (black filled circles) and two ionized-gas components of NGC 1366 were taken along the minor axis (cyan open triangles and violet filled triangles). (Morelli et al. [2017])

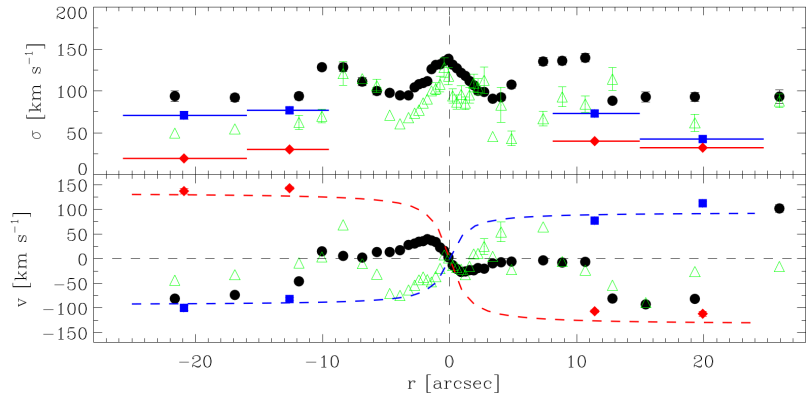


Figure 2.9: Upper panel: line-of-sight velocity dispersion; Lower panel: radial velocity profile; calculated along the major axis of NGC 1366 for the co-rotating (red filled diamonds), counter-rotating (blue filled square), total (black filled circles) stellar components and for the ionized gas component (green open triangles). The counter-rotating and co-rotating components were measured using radial bins, which are indicated by the blue and red horizontal lines in the top panel, respectively. The counter-rotating and co-rotating components' velocity rotation curves are roughly depicted by the blue and red dashed lines in the bottom panel, respectively.(Morelli et al. [2017])

Chapter 3

Instrumentation

Astrophysicists are currently working on the scientific discovery of many unexpected things in the Universe (e.g. dark matter and dark energy). These discoveries are often made by pushing the boundaries of current theories and by using powerful telescopes and/or opening new areas of instrumental technology in order to view the cosmos at different wavelengths. MUSE is designed to extend the VLT to its limit and to open a new parameter space in terms of sensitivity, spatial resolution, field of view and simultaneous spectral coverage.

3.1 Very Large Telescope

The ESO’s Very Large Telescope (VLT) is a ground based astronomical observatory which is the world’s most advanced optical telescopes, which consists of four individual telescopes with main mirrors of 8.2m in diameter and four movable 1.8m in diameter auxiliary telescopes. These four different optical telescopes are known as Antu (UT1;The Sun),Kueyen(UT2;The Moon),Melipal(UT3;The Southern Cross), and Yepun (UT4; Venus- as evening star), which are all words for astronomical objects in the Mapuche language.

[Figure 3.1](#) shows the bird’s eye view of the Very Large Telescope. The telescopes can work together, to form a giant ‘interferometer’, the ESO Very Large Telescope Interferometer, allowing astronomers to pick up much finer details of the cosmos than would be possible with the auxiliary telescopes (ATs) or the unit telescopes (UTs) alone.A flat tertiary mirror either tilts aside to allow light to pass through the primary mirror central hole to a third instrument at the Cassegrain focus, or it diverts the light to one of two instruments at the f/15 Nasmyth foci on either side with a system focal length of 120 m. This enables quick switching between any of the three instruments to suit the observing conditions within 5 minutes. Tunnels connecting additional mirrors and the central VLTI beam-combiners can be used to transmit light. Although most instruments view a narrower field, the maximum field-of-view (at Nasmyth foci) is about 27 arcminutes in diameter, slightly smaller than the full moon.

The VLT operates at visible and infrared wavelengths. The angular resolution for a single telescope is approximately 0.05 arc-seconds. The facility can achieve an angular resolution of about 0.002 arc-second when all the telescopes are combined, and each telescope can detect objects that are approximately four billion times fainter than what can be seen with the unaided eye. The instrumentation program designed for VLT is the most powerful for a single observatory. Wide-field imagers, spectrographs, adaptive-optics-corrected cameras, multi-object spectrographs, high resolution spectrographs, and spectrographs covering a wide spectral range from ultraviolet (300 nm) to mid-infrared (20 m) wavelengths are all included in it.

The 8.2-metre telescopes are protected in compact, thermally controlled structure, that rotate synchronously with the telescopes. The building are outlined in such a way that it minimizes any negative effects on the observing conditions like air turbulence in the telescope tube, which might occur due to the change in temperature and wind flow. The VLT has had a great effect on observational astronomy. It is the most powerful single ground-based facility, and results from the VLT have led to the publication of an average of more than one peer-reviewed scientific paper being published every day. The VLT has sparked a new era of scientific discovery, which includes the first image of an exoplanet, tracing the motion of individual stars around the supermassive black hole at the center of the Milky Way, and observing the gamma-ray burst's afterglow at its farthest known location.

The four 8.2-meter Unit Telescopes are capable of being combined in the VLTI, but they are primarily used for individual observations and are only accessible for interferometric observations on a limited number of nights each year. But the VLTI is able to run every night thanks to the four smaller, specialized Auxiliary Telescopes (ATs). The ATs are set up on track in such a way that they can move accurately with the observing positions from which the light beams collected by the telescope are combined in the VLTI. The ATs are very unique telescopes because they move with their own electronics, ventilation, hydraulics, and cooling systems and are self-contained in their incredibly small protective domes. A transporter on each AT lifts and moves the telescope from one place to another.

3.2 MUSE Spectrograph

The Multi Unit Spectroscopic Explorer (MUSE;[Bacon et al. \[2006\]](#)) is a second-generation instrument installed on the Nasmyth focus of UT4 at the Very Large Telescope (VLT) of the European Southern Observatory (ESO) in Paranal, Chile. It has a large field-of-view (FOV: $1' \times 1'$) panchromatic optical ($\sim 4600 - 9300\text{\AA}$) instrument with a Wide Field Mode (WFM) resolving power ranging $R = 1770 - 3590$ and a pixel scale of $0.2''$. [Figure 3.2](#) shows the image of MUSE. It has 24 Integral Field unit (IFU) models and each of them is pro-



Figure 3.1: Bird's eye view of the Very Large Telescope. Credit: J.L. Dauvergne & G. Hüdepohl

vided with a $4K \times 4K$ CCD. Moreover, the spectral range of MUSE is between 4500 and 9300 Å, and data sampled per pixel is 1.25 Å, with a spectral resolution of 2.6 Å. Therefore, each data cube of MUSE has $\sim 10^5$ spectra. The NGC1366 data were observed with the wide field mode of MUSE which has a $1' \times 1'$ field of view and without using adaptive optics, it produced data sampled at 0.2" pixels when seeing naturally.

The 3D data cube of MUSE is made up of spaxels, also known as spatial pixels, each of which contains spectral information about the galaxy. Each layer of the datacube represents the image of the observed galaxy at each wavelength in the spectral range of 4500 to 9300 Å, as can be seen from the [Figure 3.3](#), creating up to $10^4 - 10^5$ spectra in every datacube.

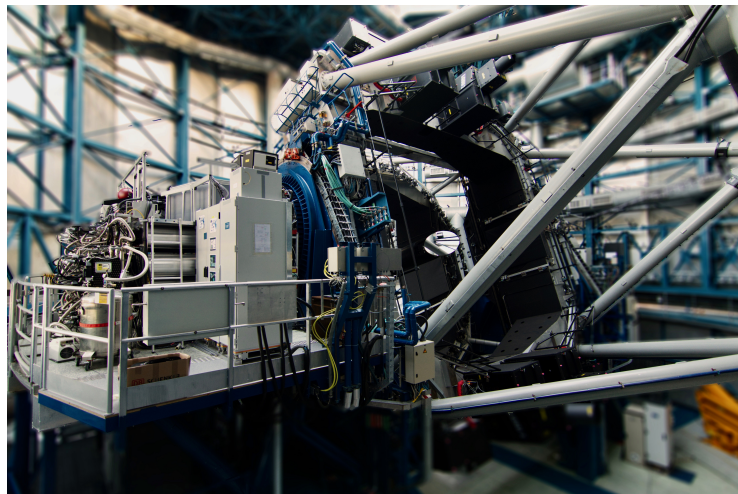


Figure 3.2: MUSE and UT4 in focus, image by R. Bacon

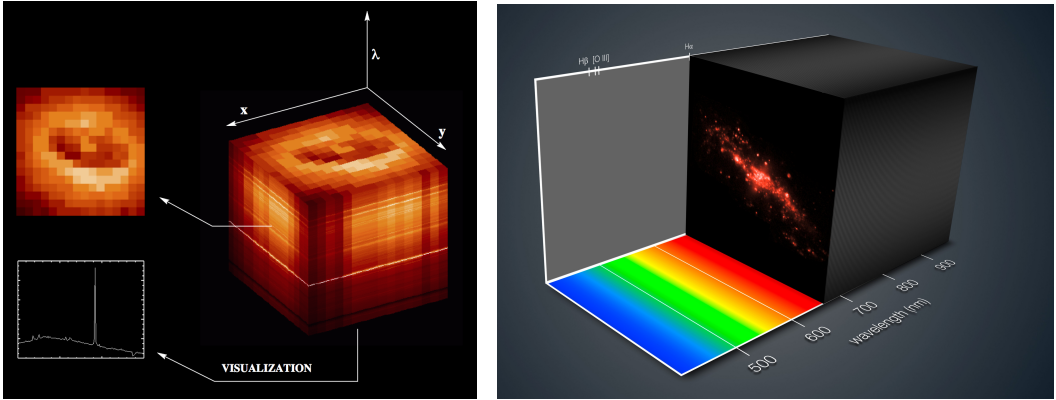


Figure 3.3: The conceptual approach of a MUSE 3D spectroscopy datacube shows the spatial axes along the x and y-axis and the spectral (λ) axis along the z-axis.

MUSE has three operating modes: a wide field mode (WFM) with and without adaptive optics correction and a narrow field mode (NFM) with adaptive optics. The observational parameters are given in table 3.1. In contrast to the wide field mode, narrow-field mode science is mainly useful for the study of single objects at extremely high spatial resolution. For instance, the study of the environment around supermassive black holes in nearby galaxies, the sphere of influence of the black holes in the most massive galaxies in the Virgo cluster, and in the coma cluster of galaxies. Additionally, MUSE NFM enables us to investigate the various solar system bodies at a spatial resolution that is comparable to more expensive space missions. Its uses include the spectroscopic study of Titan’s atmosphere, the atmospheres of Uranus and Neptune, and the internal structure and composition of comets and asteroids.

The data reduction of MUSE involves several steps, which are described below. In particular, the MUSE pipeline is used to initially process the raw data [Weilbacher et al. \[2015\]](#), and following this, two different packages are used to post-process each individual exposure: CUBEXTRACTOR ([Cantalupo et al. \[2019\]](#) for a description) and MPDAF [Piqueras et al. \[2017\]](#) to enhance the quality of final data cubes. Over the past few years, scientists have widely used this software on a large scale (examples: [Marino et al. \[2018\]](#), [Feruglio et al. \[2019\]](#), [Nanayakkara et al. \[2019\]](#), [Lusso et al. \[2019\]](#)).

Spectral range(simultaneous)	$0.465 - 0.93 \mu m$
Resolving power	20000 @ $0.46 \mu m$ 40000 @ $0.93 \mu m$
Wide Field Mode(WFM)	
Field of View	$1 \times 1 arcmin^2$
Spatial sampling	$0.2 \times 0.2 arcmin^2$
Spatial resolution(FWHM)	$0.3 - 0.4 arcmin^2$
AO condition of operation	70%-ile
Sky coverage with AO	70% at galactic pole 99% at galactic equator
Limiting Flux in 80h	$3.9 \times 10^{-19} ergs^{-1} cm^{-2}$
Narrow Field Mode(WFM)	
Field of View	$7.5 \times 7.5 arcsec^2$
Spatial sampling	$0.025 \times 0.025 arcsec^2$
Spatial resolution(FWHM)	$0.030 - 0.050 arcsec^2$
Strehl ratio	10-30%
Limiting Flux in 1h	$2.3 \times 10^{-18} ergs^{-1} cm^{-2}$
Limiting magnitude in 1h	$R_{AB} = 22.3$
Limiting surface brightness 1h	$R_{AB} = 17.3 arcsec^2$

Table 3.1: MUSE: Observational Parameters.

3.3 Spectroscopy

One of the most useful and favorite methods for understanding the cosmos is spectroscopy. It is very difficult to understand the planets, stars, galaxies, and other astronomical objects as they are very far away from us. Fortunately, the light we can see through a telescope contains a lot of crucial information about these far-off bodies. To understand the light message, it must pass through a split into different colours (or wavelengths), similar to how raindrops scatter light to create a rainbow. In the beginning, everyone was familiar with the rainbow, which is the white light of the sun dispersed into the spectrum. It was Isaac Newton (1643–1727) who made the first discovery that a prism could disperse sunlight into a continuous spectrum of colour. This research was furthered by Joseph von Fraunhofer (1787-1826), who identified and described the dark bands that, when sufficiently dispersed, can be seen in the sun’s spectrum. These dark bands were completely understood through the work of Gustav Kirchhoff (1824-1887) and Robert Bunsen (1811-1899), which resulted from the cooler gases at the surface of the sun’s surface selectively absorbing a continuous spectrum produced by the sun’s hot interior. Fraunhofer and Angelo Secchi (1818–1878), who can both be credited with founding the science of astronomical spectroscopy, made the first visual observations of the spectra of stars. [Figure 3.4](#) shows the absorption, continuum and emission spectrum.

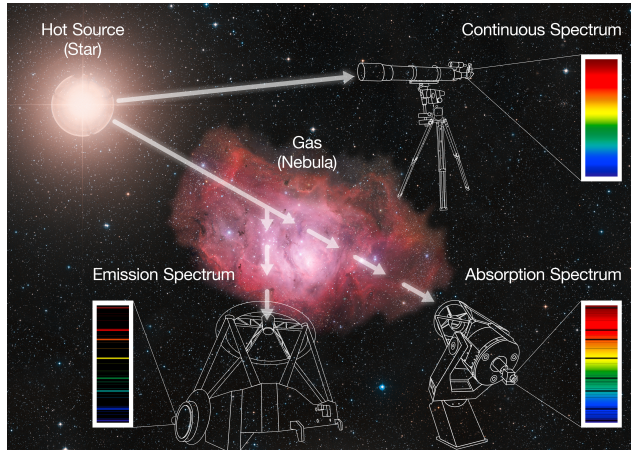


Figure 3.4: A star emits light across the spectrum — a continuum. When white light goes through a prism, it forms a rainbow, its spectrum. In the same way, as light from a star goes through the gas of a nebula — or even just the atmosphere of the star — specific colours (or wavelengths) are absorbed by the elements contained in the gas, producing dark lines over the continuum. This is an absorption spectrum. The energy that is absorbed by the gas is then re-emitted in all directions, also at the specific colours characteristic of the elements present in the gas, producing bright lines at certain wavelengths; this is known as an emission spectrum. Credit: ESO

The next two section 3.3.1 and 3.3.2 explains the main spectroscopy techniques used to study the kinematic measurements of the stellar and ionized gas components.

3.3.1 Long-Slit Spectroscopy

Long-slit spectroscopy (one-dimensional) was the most effective observational technique in the past, and even today its use has not stopped in astronomy. Generally, a spectrograph consists of four main components: a slit, a collimator, a dispersing element (prism, diffraction grating, grism), and a CCD camera. Figure 3.5 shows the optical diagram of the working of a long-slit spectrograph. The slit is placed in the focal plane and is perpendicular to the direction that the grism will direct light in. Basically, it works as a mask that only allows a thin strip of light to pass through. The strip of light that is fed into the spectrograph is what will be examined. The dispersing element “widens” the light after it passes through the collimator, which converts it into a parallel beam by deflecting the different photons at angles that depend on their wavelength. The light strip now transforms into an image that the CCD camera focuses on and records. Additionally, the slit must be smaller than the seeing disk for effective radial velocity work (so that the entire slit width is filled with starlight), but for faint stars, one may want to use a wider

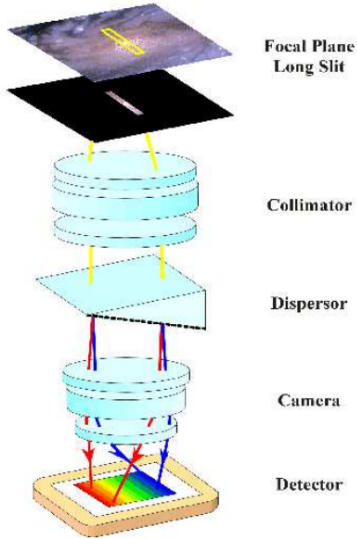


Figure 3.5: From top to bottom, in the figure, the focal plane with the galaxy’s image; the slit that allows only a galaxy’s light streak to pass through; The collimator, the grism, which deviates light according to wavelength (each wavelength will be deviated by a specific angle); the collimator, which concentrates the grism’s output spectrum on the CCD; and the CCD.

slit (to get more starlight into the system). In practice, consider the slit as a collection of small adjacent openings uniformly distributed along the slit. The resultant spectrum can be thought of as a series of one-dimensional spectra, each of which is connected to the light passing through a particular small opening. We can therefore obtain spectroscopic data—and consequently kinematic information—along a galaxy’s axis using long slit spectra. I can claim to only have one-dimensional knowledge. Generally, a spectrograph is oriented in such a way that the slit is at the center of the target galaxy, aligned with its major axis. The main function of the collimator is to generate a parallel light ray for the diffraction grating. It is very important to match the collimator and telescope optics. The collimator can be crowded, which would cause a clear loss of light, or under-filled, causing a reduction in resolution. The preferred dispersing element is typically a grating or dispensor. The resultant spectrum is focused by the camera onto the detector. Most often, a Schmidt or Maksutov type of camera is used. The detector is usually a CCD (or CCDs).

3.3.2 Integral Field Spectroscopy

Integral-field spectroscopy is a technique used in optical astronomy to create a 3D data cube of a galaxy with two spatial dimensions (x, y), one spectral dimension (λ) also known as 3D spectroscopy¹. Nowadays, IFS has become an important tool in observational astronomy to study extended objects. It has numerous benefits over the normal long-slit technique. For instance, minimal slit losses, no requirement for precise target acquisition, and ease of removing atmospheric dispersion effects. As a result of all these advantages, IFS has created many new opportunities for astronomical research, like the 2D spectroscopic study of various types of galaxies, nuclear regions of active galactic nuclei (AGN), stellar clusters, supernova remnants, planetary nebulae, star-formation regions, and so on. [Figure 3.6](#) shows the principle of IFS.

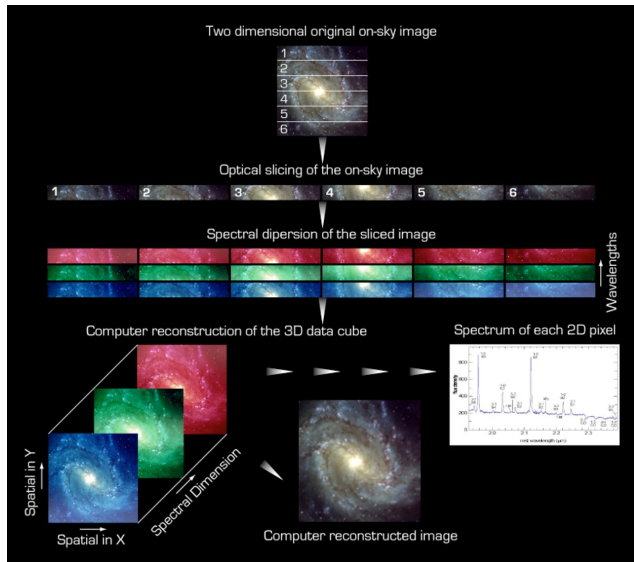


Figure 3.6: The schematic diagram of Integral field spectroscopy, Credit: ESO

In the last two decades, the instrumentation for IFS has evolved significantly, and although several methods for using this technique have been developed, the most popular one is to use an integral-field spectrograph. An appropriate optical interface is used to connect two conceptually distinct entities that make up a general integral-field spectrograph. The first is a spatial unit, called an Integral Field Unit (IFU), which receives the signal from each cell or pixel in the field and produces a spectrum for each individual pixel. All the spectra that are produced are structured into a datacube that includes the entire 2D field of view in addition to the third dimension obtained from the spectrograph, which separates the light into its various colors or wavelengths.

¹Obviously, it should be either 2D spectroscopy or possibly 3D imaging.

[Figure 3.7](#) shows the function of IFU. The second device is a spectrograph, which separates and records the spectra of each spatial element separately, that is, without any overlap.

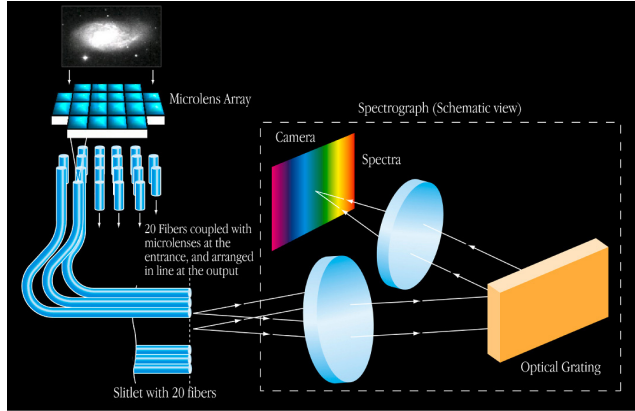


Figure 3.7: Working of IFU: Each IFU has a microlens that directs light from a small area of the sky that is typically focused on a celestial object (such as a far-off galaxy) and sends it to the spectrograph's entry (shown within the dotted box), Credit: ESO

Several existing and upcoming integral field spectrographs use one of the two most common IFU configurations as shown in [Figure 3.8](#), namely:

- (i) Image-slicer method [Richardson et al. \[1984\]](#) pioneered by Max Planck Institute for extraterrestrial Physics (MPE) with the instrument "3D" [Krabbe et al. \[1997\]](#) e.g: MUSE on the Very Large Telescope (VLT,[Bacon et al. \[2006\]](#)), Mid-Infrared Instrument(MIRI) on the James Webb Space Telescope [Krause et al. \[2008\]](#), An Image Slicer-IFU installed in the Penn State near-IR imager and spectrograph (PIRIS,[Ren and Ge \[2003\]](#)).
- (ii) Optical fiber array: e.g; PMAS on the Calar Alto Telescope [Roth et al. \[2005\]](#), GMOS-IFU on the Gemini-North Telescope [Allington-Smith et al. \[2002\]](#), and SPIRAL IFU on the Anglo-Australian Telescope (AAT, [Kenworthy et al. \[2001\]](#)).

Integral field units (IFUs) made with fiber optics offer a great deal of flexibility in terms of both their design and where they are placed in relation to the spectrographs they feed. In order to minimize the gaps between the spaxels caused by the cladding of the fiber optics, a fiber array IFU typically has a microlens array as the fore-optics (kOALA; [Ellis et al. \[2012\]](#)). but it is not necessary in any way (e.g. PPak; [Kelz et al. \[2006\]](#)). The CALIFA Survey [Sánchez et al. \[2012\]](#), which used the PPak instrument to observe 600 galaxies over 250 nights, is one of the largest integral-field galaxy surveys to date. One of the constraints on the advancement of studies on galaxy evolution is the typical survey speed of integral field spectrographs, which is less than two galaxies per night. The use of fiber optics enhances the ability to

perform precise sky subtraction by designating some of the fibers in the slit as dedicated sky fibers dispersed from the IFU on the focal plane. The other IFU designs are unable to accomplish this, despite the fact that MUSE and other similar instruments have a sufficiently wide fields of view to guarantee that a sizable portion of their spaxels are always devoted to sky observation [Streicher et al. \[2011\]](#). Integral-field spectroscopy has provided deeper parameter spaces

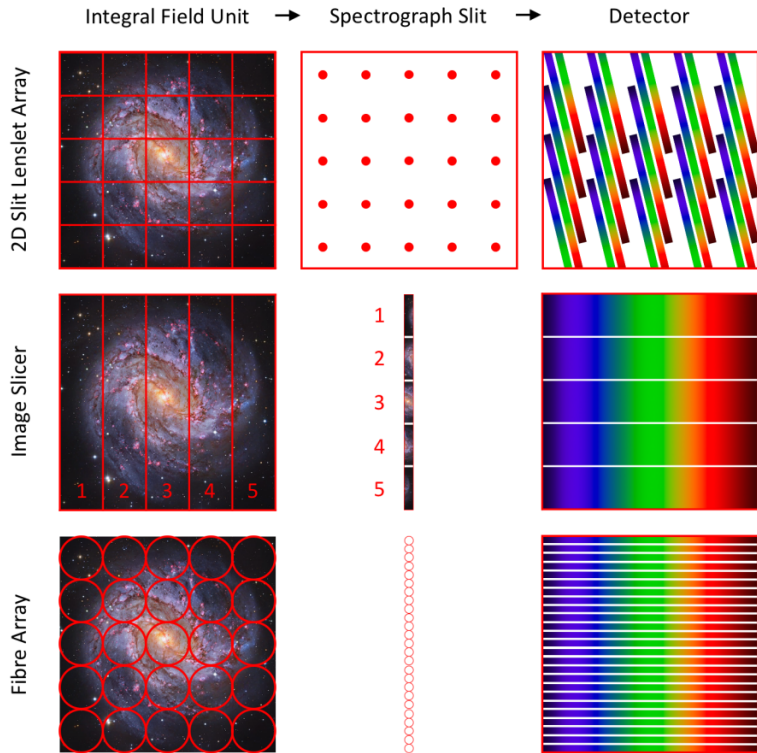


Figure 3.8: The figure explains the integral-field spectrograph designs: 2D slit at the top, image slicer in the middle, and fiber array at the bottom. The integral-field unit is projected in the first column on the sky, the spectrograph’s entrance slit is formatted in the second column, and the dispersed spectra are projected in the third column on the detector ([Allington-Smith and Content \[1998\]](#) [Oswalt and McLean \[2013\]](#)).

for probing the physics of galaxies by providing spatial information about a galaxy’s ionization, stellar characteristics, and velocity field. Edge-on galaxies’ discs are seen being dramatically pushed off by AGN/starburst winds [Sharp and Bland-Hawthorn \[2010\]](#),[Ho et al. \[2014\]](#). The merging history of a galaxy can be investigated using gradients revealed by stellar population analysis [Rawle et al. \[2008\]](#)[Pracy et al. \[2013\]](#). Along with probing a galaxy’s local dark matter content, the velocity fields exhibit dynamic traces of its interaction history [Krajnović et al. \[2011\]](#),[Khochfar et al. \[2011\]](#),[Cecil et al. \[2015\]](#).

Chapter 4

Results and Discussions

In this chapter, I have explained my thesis work and results, [section 4.1](#) presents the observation details of the NGC 1366 galaxy; [section 4.2](#) explains the data reduction and binning methods. The emission line spectra of the galaxy in [section 4.3](#). The investigated kinematics and flux 2D maps of the emission-line gases in the galaxy are in [section 4.4](#). The measured flux ratio maps and their variation from the center of the galaxy are in [section 4.5](#). Finally, in [section 4.6](#) the conclusion of the results are discussed.

4.1 Observation of NGC 1366

The spectroscopic observational data of NGC 1366 were taken in August 2019 using the MUSE, the optical integral field unit (IFU) on the Very Large Telescope (VLT). The reduced data is also available in the ESO Science Archive at <http://archive.eso.org/cms.html> and can be accessed with program ID 0103.B-0331(A) (P.I: Lorenzo Morelli). The wide-field mode ensured a field of view of $1 \times 1 \text{ arcmin}^2$ with a spatial sampling of $0.2 \times 0.2 \text{ arcsec}^2$. The wavelength range from 4650 to 9300 Å was covered with a spectral sampling of 1.25 Å per slice and a nominal spectral resolution of $FWHM_{inst} = 2.5\text{\AA}$ at 7000 Å. The measured spectral resolution was on average $FWHM_{inst} = 2.8\text{\AA}$ with little variation ($<0.2 \text{ \AA}$) with wavelength and position over the field of view. With the help of MUSE's high-quality spectroscopic data, it is possible to make a huge number of measurements about the characteristics of the gas and stellar components. In order to cover the whole galaxy we needed a mosaic of four single MUSE pointings. Each single pointing was about 40 minutes on-target integration time covering one of the four quadrants of the galaxy. There was an overlap of 10'' between nearby quadrants so that the resulting field of view of the MUSE observations was $(110'' \times 110'')$ (see [Figure 4.1](#)). We measured the kinematics of the ionized gas across the galaxy's surface using the spectra in the MUSE data cubes in order to comprehend the three-dimensional structure of the galaxy.

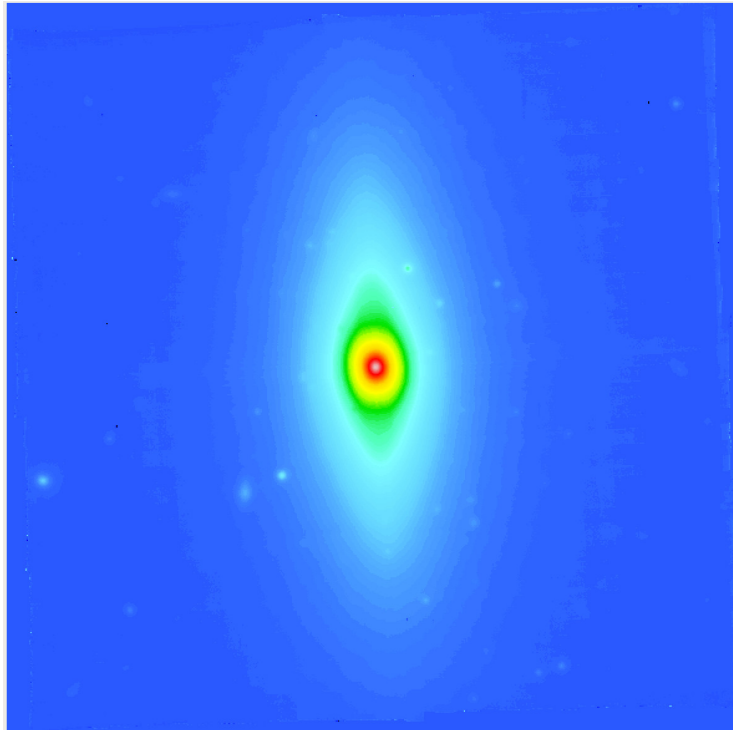


Figure 4.1: Reconstructed image of NGC 1366 (Size=110" × 110").

4.2 Data Reduction and Binning Method

The data reduction was performed with the MUSE pipeline version 2.2 Weilbacher et al. [2016] under the ESOREFLEX environment Freudling et al. [2013]. The main steps included bias and overscan subtraction, flat fielding to correct the pixel-to-pixel response variation, wavelength calibration, determination of the line spread function, and illumination correction (using a twilight exposure). By using the dedicated sky frames, the sky subtraction was done by fitting and subtracting a sky model spectrum on each spaxel of the field of view. The flux calibration and the first-order correction of the atmospheric telluric features were obtained using the spectro-photometric standard star observed at twilight. The continuum spectrum of NGC1366 was derived by applying a pPXF Cappellari [2012] fitting. It was used the Library of Empirical Spectra library (MILES) with the canonical base models BaseFe Vazdekis et al. [2012], with instrumental FWHM = 2.54 Å. All emission lines have been masked by the fitting algorithm. The spectrum of each spaxel with sufficient S/N of the MUSE field of view has been fitted deriving the stellar kinematics and the best stellar template spectrum. For each position on the galaxy we have therefore a stellar continuum constructed with the appropriate shift and broadening and with the best stellar spectra composition. This was possible only in the region of the galaxy where the S/N allowed such measurements. Figure 4.2 shows the stellar continuum subtraction.

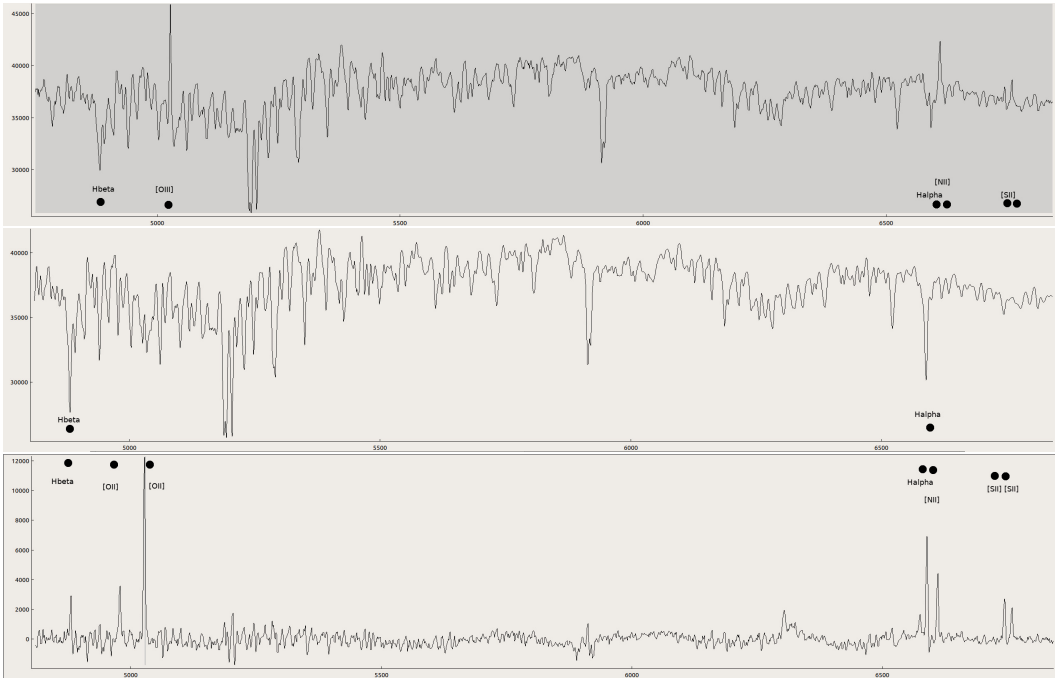


Figure 4.2: Upper image is the original spectrum of the galaxy, Middle image is the continuum spectrum which is the result of a pPXF spectral fitting that used the MILES stellar libraries [Cappellari \[2012\]](#), Bottom image is the emission line spectrum which is the result of stellar continuum subtraction.

The term "binning" refers to the average of observations taken at different positions on the sky (i.e., different pixels), rather than along the spectral direction. It is performed to increase the SNR and easy to extract the information from the data with less computational power. The binning method in 1D is simple to use: one only needs to ensure that every bin is close to every other one and that their S/N reaches a minimum value. While in 2D (and higher dimensions), as the shape of the bin must then be taken into consideration, which is quite a complex process. For the binning of the 2D data, [Cappellari and Copin \[2003\]](#) describes in detail the methods and algorithms called the voronoi binning method, which adaptively bins data into regions of constant signal-to-noise ratio per bin. This method is very useful to examine the spectra from the MUSE data because the quality and signal-to-noise ratio varied across the data cube.

In order to study the stellar continuum in the galaxy, Voronoi binning is primarily employed due to the constant or comparable signal-to-noise throughout the entire field. In our case, we were interested in studying the gas of the galaxy and in a region where there is no continuum signal. We have a signal outside the galaxy, so we cannot apply the voronoi binning method in the NGC 1366. We have used the normal binning, The first binned data we

started to work had 121 spectra of each has 50x50 spaxel size. At the end, we realised that with 50 spaxel the information was not revealed therefore we again binned the data with 10x10 spaxel. The results for this thesis are studied by using the 10x10 spaxel binning.

4.3 Emission line spectra

The emission lines are bright lines or lines of increased intensity on a continuous spectrum. The main processes for the emission of radiation are from the discrete processes, generated only by bound-bound transitions, and continuous processes, which arises from free-free, free-bound and bound-free transitions. Thermal (Doppler) broadening, intrinsic broadening, and collision broadening are the physical processes that broaden the spectral lines. To examine the ionized gas in the NGC 1366, I have used mainly H α ($\lambda = 6562.80$), H β ($\lambda = 4861.31$), [OIII]($\lambda = 5006.83$) and [NII]($\lambda = 6583.41$) emission lines because these lines are the only dominated lines as compared to others like [OIII]($\lambda = 4958.92$), [SII]($\lambda = 6716.47, 6730.85$) and so on. To analyse the emission line flux, relative velocity and velocity dispersion I got 3364 spectra which corresponds to the 3364 bins of 10x10 spaxels. For the best fitting of the emission lines, I have used gaussian line profile and least square fitting methods. Out of 3364 spectral best fittings, [Figure 4.3](#) and [Figure 4.4](#) shows the best fit for the emission line of H β , H α and [OIII], [NII]. The value I got from analysing the spectra were put back into the pixels to attain the 2D maps.

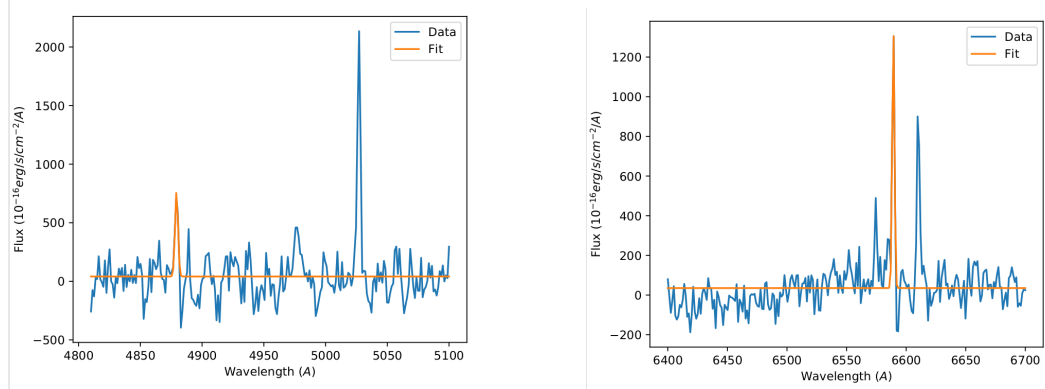


Figure 4.3: The H β ($\lambda = 4861.31$) (Left) and H α ($\lambda = 6562.80$) (Right) emission line of the NGC 1366 galaxy, The Muse spectra (blue) and the best fit (orange).

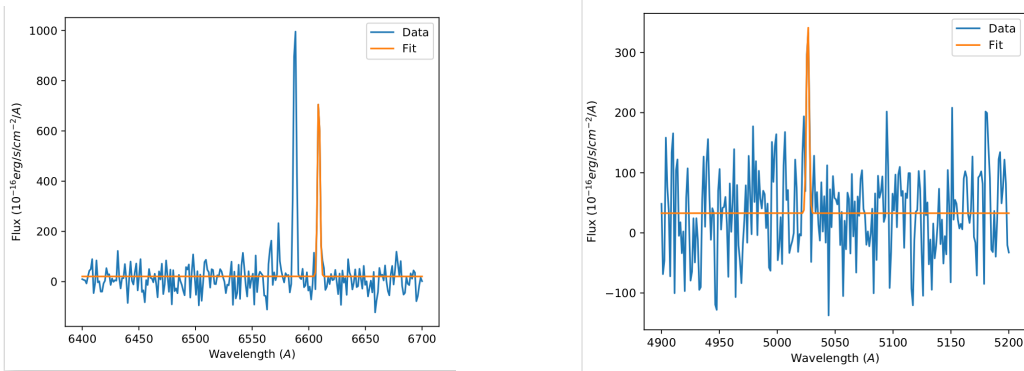


Figure 4.4: The [NII] $(\lambda = 6583.41)$ (Left) and [OIII] $(\lambda = 5006.83)$ (Right) emission line of the NGC 1366 galaxy, The Muse spectra (blue) and the best fit (orange).

4.4 Flux Distribution and Kinematical Fields

The kinematic and flux maps of the emission-line gasses that are spatially resolved are given in the Figure 4.5 and Figure 4.6. Only those bins with a signal-to-noise ratio (SNR) >3 are plotted.

The first, second and third column represent the emission line flux, relative velocity and velocity dispersion respectively. At the center of the galaxy velocity dispersion is dominated which is also true for at a distance of 1.64 kpc right to the center. The emission line flux for the [NII] is maximum, and all the fluxes have some sort of erratic spiral structure. The H β flux are the weakest and least abundant emission lines, and they appear to exist mostly in the very center of the galaxy. The detection of these weaker lines is relatively limited by the short exposure of the MUSE cube, poor seeing conditions and high illumination from the Moon during the observations.

At larger radii the gas has a filamentary structure and less velocity dispersion. In the relative velocity maps, there is no uniform motion around the center of the galaxy. In the blue shifted part of the galaxy, we see the small red shifted blobs, while in the red shifted part of the galaxy, we see the small blue shifted blobs. Moreover, relative velocity along the major axis is the same as observed by Morelli et al. [2017](see Figure 2.9). Through maps, It is clear that at the center of the galaxy the gas has irregular motion. This may imply the existence of a second gas component that rotates in opposition to the major gas components or that the gas components rotate alongside the original stellar components. If this is the case, there might be two counter-rotating gaseous components. If so, it might be the cause of the gas's high velocity dispersion at a radius of approximately 1.64 kpc in the upper left corner of the maps.

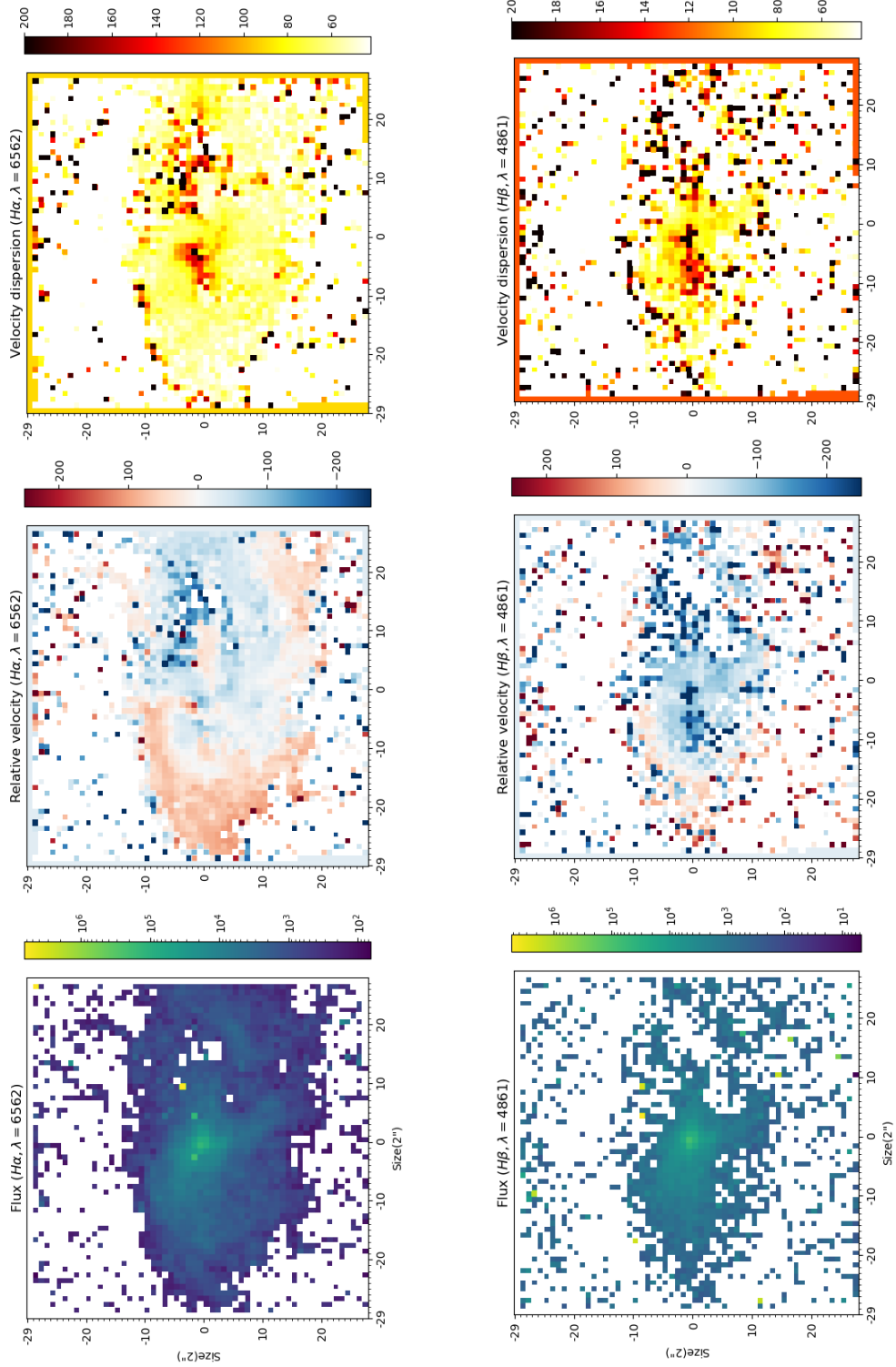


Figure 4.5: The maps of emission-line flux, relative velocity and velocity dispersion for H α (First column) and H β (Second Column).

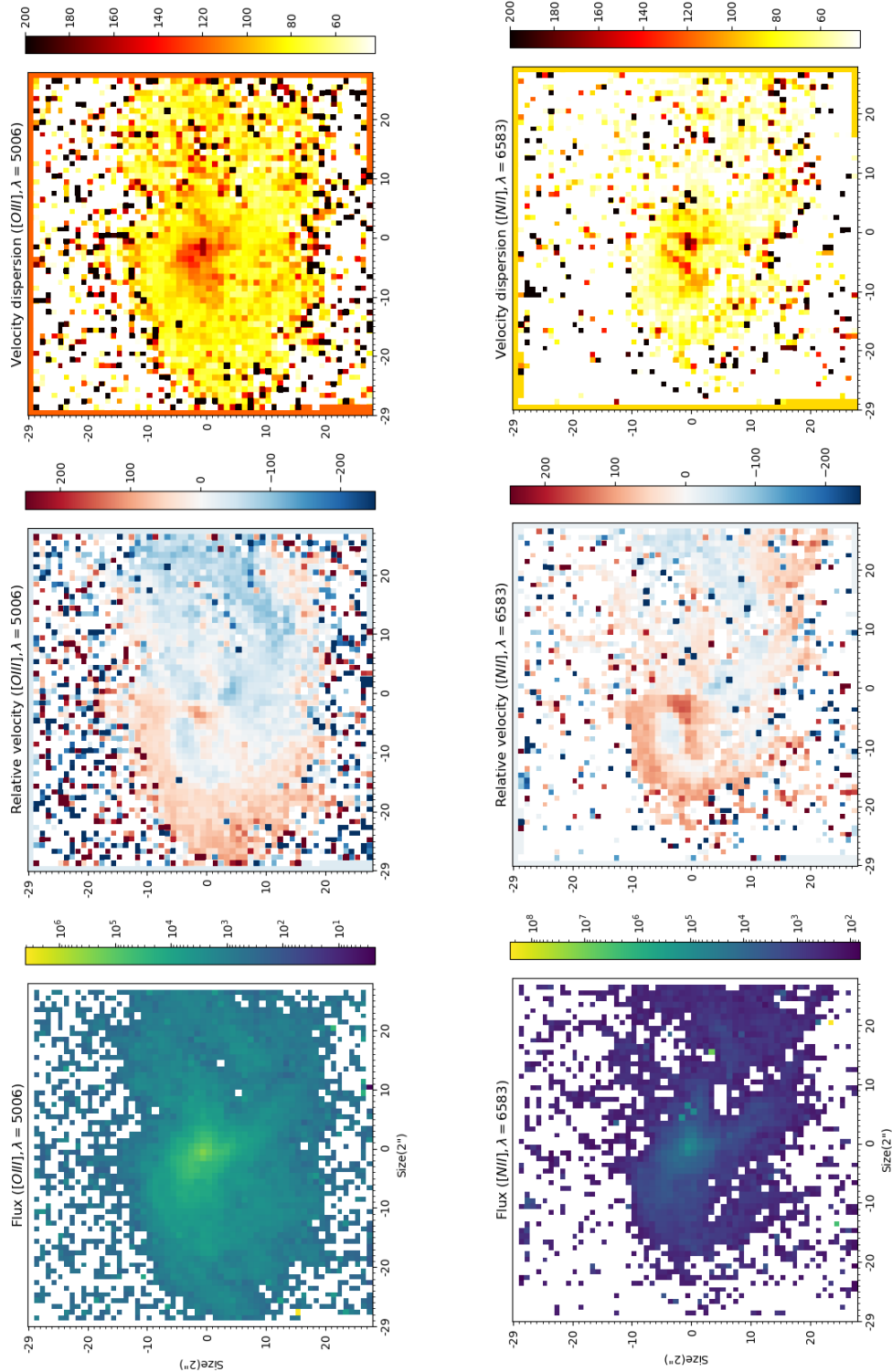
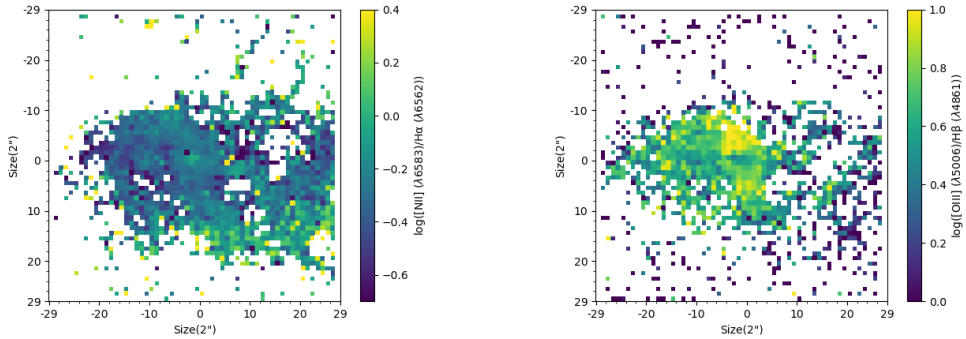


Figure 4.6: The maps of emission-line flux, relative velocity and velocity dispersion for $[\text{O}/\text{H}]$ (First column) and $[\text{N}/\text{H}]$ (Second Column).

4.5 Ionization Mechanism of Nebular Gas

It is important to understand the characteristics of the ionized gas along with flux analysis and kinematic data of the gas. The "Baldwin, Phillips & Terlevich" (BPT) diagram, which is the study of the flux ratios of $\log([\text{OIII}]/\text{H}\beta)$ and $\log([\text{NII}]/\text{H}\alpha)$, is the most common method for determining the mechanism of gas ionization.

The flux ratio maps of the NGC 1366 are shown in the figure [Figure 4.7](#). From the analysis of $\log([\text{NII}]/\text{H}\alpha)$ (left panel map), It is clear that [NII] and H α are almost uniformly distributed at the center of the galaxy. From the analysis of $\log([\text{OIII}]/\text{H}\beta)$ (right panel map), It is obvious that [OIII] dominates the galaxy more than H β and is maximum at the center. Moreover, H α has more negative value than H β in the maps.



[Figure 4.7](#): $\log([\text{NII}]/\text{H}\alpha)$ (left panel) and $\log([\text{OIII}]/\text{H}\beta)$ (right panel) maps of NGC 1366.

The [Figure 4.8](#) depicts the flux ratio plotted against the distance from the center of the galaxy. The measured flux ratio of $\log([\text{NII}]/\text{H}\alpha)$ is almost constant about ~ 3 kpc and H α has negative value which is true in correspondence to the map of $\log([\text{NII}]/\text{H}\alpha)$ ratio. The measured flux ratio of $\log([\text{OIII}]/\text{H}\beta)$ is heavily distributed and gradually decreasing from the central region to ~ 2 kpc and H β has almost positive value which is true in correspondence to the map of $\log([\text{OIII}]/\text{H}\beta)$ ratio. At larger radii, the flux has not uniform distribution, where the S/N ratio is lower. Moreover, It concludes that H α and H β flux are lower than compared to the nitrogen ([NII]) and oxygen [OIII].

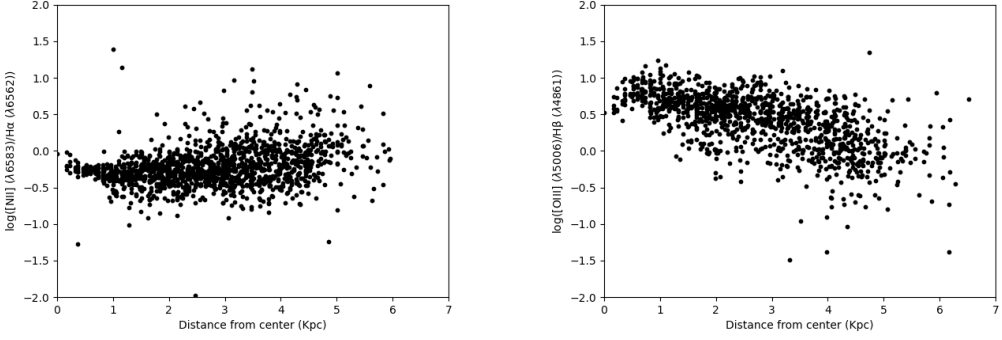


Figure 4.8: $\log([\text{NII}]/\text{H}\alpha)$ (left panel) and $\log([\text{OIII}]/\text{H}\beta)$ (right panel) plotted against the distance from the center of the galaxy.

To classify ionization mechanism of gas in NGC 1366, we have used $\log([\text{NII}]/\text{H}\alpha)$ and $\log([\text{OIII}]/\text{H}\beta)$ line ratios, which is called (BPT) diagram as shown in Figure 4.9. It shows how to distinguish LINERs from typical H II regions and AGNs (Seyferts and QSOs). The categories, we use Equation 4.1 derived from Kauffmann et al. [2003] which implies that the star-forming systems are located below Equation 4.1 while above this are called LINERs. Therefore, It is clearly seen that there is no sign of star formation in the NGC 1366.

$$\log([\text{OIII}]/\text{H}\beta) = \frac{0.61}{\log([\text{NII}]/\text{H}\alpha) - 0.05} + 1.30 \quad (4.1)$$

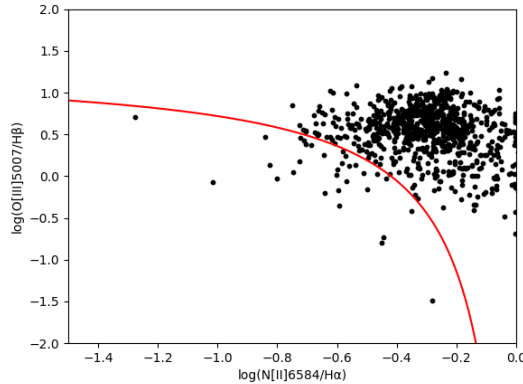


Figure 4.9: Diagnostic diagrams of NGC 1366, $\log([\text{NII}]/\text{H}\alpha)$ (Horizontal) and $\log([\text{OIII}]/\text{H}\beta)$ (vertical).

4.6 Discussion and conclusions

In this work we have investigated the ionized gas in the NGC 1366. We used IFU data from MUSE to study spatially resolved structure, flux, and kinematics of the gas emission lines. We extracted the gas information from the MUSE data cube and make the 2D maps for the emission line flux, relative velocity and velocity dispersion. Moreover, we used flux ratios to understand how the ionized gas is distributed in the galaxy. Our key findings are outlined below.

Our analysis confirms the main results about the gas by Morelli et al. [2017]; the relative velocity along the major axis has same values and irregular motion at the center of the NGC 1366. Also, outside the center of the galaxy the gas has irregular motion with velocity similar to the previous results.

The most prominent lines in the optical region of NGC 1366 are $H\alpha$, [OIII]($\lambda = 5006.83$), [NII]($\lambda = 6583.41$) and $H\beta$. The structure of these flux lines appear to be in a spiral-like structure or elongated features along the galaxy's major axis.

By analysing the ionization mechanism in section 4.5 We determined that the nitrogen [NII] and oxygen [OIII] are stronger than the $H\alpha$ and $H\beta$, which means there is no star formation in this galaxy. This give an explanation of the failed detection of CO lines. Indeed, we observed in 2020 NGC 1366 by the Atacama Pathfinder Experiment (APEX) telescope to find the signature of carbon monoxide (CO) which are often related to star formation, but we didn't find anything. Therefore, it is clear that there is no star formation in the NGC 1366.

[Figure 4.10](#) which is the collection of well studied published data of counter-rotating galaxy. The morphology of counter-rotating galaxies with their stellar population and of star formation. [Morelli et al. \[2017\]](#) found the age of counter-rotating and corotating stellar component are 2.6 Gyr and 5.6 Gyr. Therefore, it is confirmed that NGC 1366 is a galaxy with no star formation.

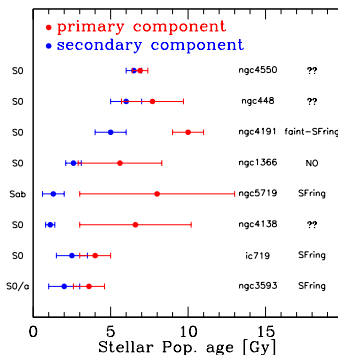


Figure 4.10: Study of the counter-rotating galaxy with their stellar population.

Bibliography

David G Algorry, Julio F Navarro, Mario G Abadi, Laura V Sales, Matthias Steinmetz, and Franziska Piontek. Counterrotating stars in simulated galaxy discs. *Monthly Notices of the Royal Astronomical Society*, 437(4):3596–3602, 2014.

Jeremy Allington-Smith and Robert Content. Sampling and background subtraction in fiber-lenslet integral field spectrographs. *Publications of the Astronomical Society of the Pacific*, 110(752):1216, 1998.

Jeremy Allington-Smith, Graham Murray, Robert Content, George Dodsworth, Roger Davies, Bryan W Miller, Inger Jorgensen, Isobel Hook, David Crampton, and Richard Murowinski. Integral field spectroscopy with the gemini multiobject spectrograph. i. design, construction, and testing. *Publications of the Astronomical Society of the Pacific*, 114(798):892, 2002.

Roland Bacon, Svend Bauer, Petra Böhm, Didier Boudon, Sylvie Brau-Nogué, Patrick Caillier, Lionel Capoani, C Marcella Carollo, Nicolas Champavert, Thierry Contini, et al. Probing unexplored territories with muse: a second generation instrument for the vlt. In *Ground-based and Airborne Instrumentation for Astronomy*, volume 6269, pages 183–191. SPIE, 2006.

F Bertola and M Capaccioli. Dynamics of early type galaxies. i-the rotation curve of the elliptical galaxy ngc 4697. *The Astrophysical Journal*, 200:439–445, 1975.

F Bertola, LM Buson, and WW Zeilinger. The external origin of the gas in s0 galaxies. *The Astrophysical Journal*, 401:L79–L81, 1992.

Francesco Bertola and Daniela Bettoni. The counterrotation of gas and stars in the dust lane elliptical ngc 5898. *The Astrophysical Journal*, 329:102–106, 1988.

Francesco Bertola, Pierantonio Cinzano, Enrico Maria Corsini, Alessandro Pizzella, Massimo Persic, and Paolo Salucci. Counterrotating stellar disks in early-type spirals: Ngc 3593. *The Astrophysical Journal*, 458(2):L67, 1996.

- D Bettoni. Rotation axes of gas and stars in elliptical galaxies. *The Messenger*, 37:17–19, 1984.
- D Bettoni and G Galletta. A survey of the stellar rotation in barred galaxies. *Astronomy and Astrophysics Supplement Series*, 124(1):61–74, 1997.
- D Bettoni, G Galletta, and F Prada. The visible environment of galaxies with counterrotation. *Astronomy & Astrophysics*, 374(1):83–91, 2001.
- D Bettoni, G Galletta, and S García-Burillo. A new catalogue of ism content of normal galaxies. *Astronomy & Astrophysics*, 405(1):5–14, 2003.
- Daniela Bettoni. On the observed shape of the stellar rotation curve in bars. *The Astronomical Journal*, 97:79–82, 1989.
- Roelof Bottema. The kinematics of the bulge and the disc of ngc 7331. *arXiv preprint astro-ph/9902240*, 1999.
- Robert Braun, René AM Walterbos, and Robert C Kennicut. Counter-rotating gaseous disks in the “evil eye” galaxy ngc4826. *Nature*, 360(6403):442–444, 1992.
- M Bureau and A Chung. Discovery of counter-rotating gas in the galaxies ngc 1596 and 3203 and the incidence of gas counter-rotation in s0 galaxies. *Monthly Notices of the Royal Astronomical Society*, 366(1):182–188, 2006.
- Sebastiano Cantalupo, Gabriele Pezzulli, Simon J Lilly, Raffaella Anna Marino, Sofia G Gallego, Joop Schaye, Roland Bacon, Anna Feltre, Wolfram Kollatschny, Themiya Nanayakkara, et al. The large-and small-scale properties of the intergalactic gas in the slug ly α nebula revealed by muse he ii emission observations. *Monthly Notices of the Royal Astronomical Society*, 483(4):5188–5204, 2019.
- Michele Cappellari. ppxf: Penalized pixel-fitting stellar kinematics extraction. *Astrophysics Source Code Library*, pages ascl-1210, 2012.
- Michele Cappellari and Yannick Copin. Adaptive spatial binning of integral-field spectroscopic data using voronoi tessellations. *Monthly Notices of the Royal Astronomical Society*, 342(2):345–354, 2003.
- C Marcella Carollo and I John Danziger. Colours, line strengths and stellar kinematics of ngc 2663 and 5018. *Monthly Notices of the Royal Astronomical Society*, 270(4):743–768, 1994.
- Gerald Cecil, LMR Fogarty, Samuel Richards, Jonathan Bland-Hawthorn, Rebecca Lange, Amanda Moffett, Barbara Catinella, Luca Cortese, I-T Ho, Edward N Taylor, et al. The sami galaxy survey: gas streaming and dynamical m/l in rotationally supported systems. *Monthly Notices of the Royal Astronomical Society*, 456(2):1299–1319, 2015.

R Ciri, D Bettoni, and G Galletta. A massive counter-rotating gas disk in a spiral galaxy. *Nature*, 375(6533):661–663, 1995.

L Coccato, L Morelli, A Pizzella, EM Corsini, LM Buson, and E Dalla Bontà. Spectroscopic evidence of distinct stellar populations in the counter-rotating stellar disks of ngc 3593 and ngc 4550. *Astronomy & Astrophysics*, 549:A3, 2013.

Lodovico Coccato, Lorenzo Morelli, Enrico Maria Corsini, L Buson, Alessandro Pizzella, Daniela Vergani, and Francesco Bertola. Dating the formation of the counter-rotating stellar disc in the spiral galaxy ngc 5719 by disentangling its stellar populations. *Monthly Notices of the Royal Astronomical Society: Letters*, 412(1):L113–L117, 2011.

Neil F Comins, Richard VE Lovelace, Thomas Zeltwanger, and Peter Shorey. One-armed spiral waves in galaxy simulations with counterrotating stars. *The Astrophysical Journal*, 484(1):L33, 1997.

EM Corsini, A Pizzella, and F Bertola. The orthogonal gaseous kinematical decoupling in the sa spiral ngc 2855. *Astronomy & Astrophysics*, 382(2):488–494, 2002.

EM Corsini, A Pizzella, L Coccato, and F Bertola. Minor-axis velocity gradients in spirals and the case of inner polar disks. *Astronomy & Astrophysics*, 408(3):873–885, 2003a.

Enrico Maria Corsini, Victor P Debattista, and JAL Aguerri. Direct confirmation of two pattern speeds in the double-barred galaxy ngc 2950. *The Astrophysical Journal*, 599(1):L29, 2003b.

Alison F Crocker, Hyunjin Jeong, Shinya Komugi, Francoise Combes, Martin Bureau, Lisa M Young, and Sukyoung Yi. Molecular gas and star formation in the red-sequence counter-rotating disc galaxy ngc 4550. *Monthly Notices of the Royal Astronomical Society*, 393(4):1255–1264, 2009.

Timothy A Davis, Katherine Alatalo, Marc Sarzi, Martin Bureau, Lisa M Young, Leo Blitz, Paolo Serra, Alison F Crocker, Davor Krajnović, Richard M McDermid, et al. The atlas3d project–x. on the origin of the molecular and ionized gas in early-type galaxies. *Monthly Notices of the Royal Astronomical Society*, 417(2):882–899, 2011.

Tim de Zeeuw and Marijn Franx. Structure and dynamics of elliptical galaxies. *Annual review of Astronomy and Astrophysics*, 29(1):239–274, 1991.

Pierre-Alain Duc, Jean-Charles Cuillandre, Paolo Serra, Leo Michel-Dansac, Etienne Ferriere, Katherine Alatalo, Leo Blitz, Maxime Bois, Frédéric Bournaud, Martin Bureau, et al. The atlas3d project–ix. the merger origin of a

fast-and a slow-rotating early-type galaxy revealed with deep optical imaging: first results. *Monthly Notices of the Royal Astronomical Society*, 417(2):863–881, 2011.

Simon C Ellis, M Ireland, Jon S Lawrence, Julia Tims, N Staszak, Jurek Brzeski, Quentin A Parker, Robert Sharp, J Bland-Hawthorn, Scott Case, et al. Koala: a wide-field 1000 element integral-field unit for the anglo-australian telescope. In *Ground-based and Airborne Instrumentation for Astronomy IV*, volume 8446, pages 279–286. SPIE, 2012.

NW Evans and JL Collett. Separatrix crossing and the enigma of ngc 4550. *The Astrophysical Journal*, 420:L67–L70, 1994.

Maximilian H Fabricius, Roberto P Saglia, David B Fisher, Niv Drory, Ralf Bender, and Ulrich Hopp. Kinematic signatures of bulges correlate with bulge morphologies and sérsic index. *The Astrophysical Journal*, 754(1):67, 2012.

C Feruglio, G Fabbiano, M Bischetti, M Elvis, A Travascio, and F Fiore. Multiphase gas flows in the nearby seyfert galaxy eso428-g14. *arXiv preprint arXiv:1904.01483*, 2019.

David Fisher, Garth Illingworth, and Marijn Franx. The dynamics and structure of the s0 galaxy ngc 7332. *The Astronomical Journal*, 107:160–172, 1994.

W Freudling, M Romaniello, DM Bramich, P Ballester, V Forchi, CE García-Dabló, S Moehler, and MJ Neeser. Automated data reduction workflows for astronomy-the eso reflex environment. *Astronomy & Astrophysics*, 559:A96, 2013.

Daniel Friedli. Counter-rotating bars within bars. *arXiv preprint astroph/9602153*, 1996.

G Galletta. Detection of retrograde gas streaming in the sb0 galaxy ngc 4546. *The Astrophysical Journal*, 318:531–535, 1987.

AM Garcia, G Paturel, L Bottinelli, and L Gouguenheim. General study of group membership. i-the sample. *Astronomy and Astrophysics Supplement Series*, 98:7–15, 1993.

S Garcia-Burillo, MJ Sempere, and D Bettoni. First detection of a counterrotating molecular gas disk in a spiral galaxy: Ngc 3626. *The Astrophysical Journal*, 502(1):235, 1998.

S García-Burillo, MJ Sempere, F Combes, LK Hunt, and R Neri. Anatomy of the counterrotating molecular disk in the spiral ngc 3593. 12co (1-0) interferometer observations and numerical simulations. *Astronomy and Astrophysics*, 363:869–886, 2000.

Martha P Haynes, Katherine P Jore, Elizabeth A Barrett, Adrick H Broeils, and Brian M Murray. Kinematic evidence of minor mergers in normal sa galaxies: Ngc 3626, ngc 3900, ngc 4772, and ngc 5854. *The Astronomical Journal*, 120(2):703, 2000.

I-Ting Ho, Lisa J Kewley, Michael A Dopita, Anne M Medling, James T Allen, Joss Bland-Hawthorn, Jessica V Bloom, Julia J Bryant, Scott M Croom, Lisa MR Fogarty, et al. The sami galaxy survey: shocks and outflows in a normal star-forming galaxy. *Monthly Notices of the Royal Astronomical Society*, 444(4):3894–3910, 2014.

Evelyn J Johnston, Michael R Merrifield, Alfonso Aragón-Salamanca, and Michele Cappellari. Disentangling the stellar populations in the counter-rotating disc galaxy ngc 4550. *Monthly Notices of the Royal Astronomical Society*, 428(2):1296–1302, 2013.

SJ Kannappan and DG Fabricant. A broad search for counterrotating gas and stars: evidence for mergers and accretion. *The Astronomical Journal*, 121(1):140, 2001.

I Katkov, I Chilingarian, O Sil’chenko, A Zasov, and V Afanasiev. A complex stellar line-of-sight velocity distribution in the lenticular galaxy ngc 524. *Open Astronomy*, 20(3):453–458, 2011.

Ivan Yu Katkov, Olga K Sil’chenko, and Victor L Afanasiev. Lenticular galaxy ic 719: Current building of the counterrotating large-scale stellar disk. *The Astrophysical Journal*, 769(2):105, 2013.

Guinevere Kauffmann, Timothy M Heckman, Christy Tremonti, Jarle Brinchmann, Stéphane Charlot, Simon DM White, Susan E Ridgway, Jon Brinkmann, Masataka Fukugita, Patrick B Hall, et al. The host galaxies of active galactic nuclei. *Monthly Notices of the Royal Astronomical Society*, 346(4):1055–1077, 2003.

Andreas Kelz, Marc AW Verheijen, Martin M Roth, Svend M Bauer, Thomas Becker, Jens Paschke, Emil Popow, Sebastian F Sánchez, and Uwe Laux. Pmas: The potsdam multi-aperture spectrophotometer. ii. the wide integral field unit ppak. *Publications of the Astronomical Society of the Pacific*, 118(839):129, 2006.

Matthew A Kenworthy, Ian R Parry, and Keith Taylor. Spiral phase a: A prototype integral field spectrograph for the anglo-australian telescope. *Publications of the Astronomical Society of the Pacific*, 113(780):215, 2001.

Sadegh Khochfar, Eric Emsellem, Paolo Serra, Maxime Bois, Katherine Alatalo, Roland Bacon, Leo Blitz, Frédéric Bournaud, Martin Bureau, Michele Cappellari, et al. The atlas3d project—viii. modelling the formation and

evolution of fast and slow rotator early-type galaxies within λ cdm. *Monthly Notices of the Royal Astronomical Society*, 417(2):845–862, 2011.

Alfred Krabbe, Niranjan A Thatte, Harald Kroker, Lowell E Tacconi-Garman, and Matthias Tecza. 3d: a new generation imaging spectrometer. In *Optical Telescopes of Today and Tomorrow*, volume 2871, pages 1179–1186. SPIE, 1997.

Davor Krajnović, Eric Emsellem, Michele Cappellari, Katherine Alatalo, Leo Blitz, Maxime Bois, Frédéric Bournaud, Martin Bureau, Roger L Davies, Timothy A Davis, et al. The atlas3d project–ii. morphologies, kinematic features and alignment between photometric and kinematic axes of early-type galaxies. *Monthly Notices of the Royal Astronomical Society*, 414(4):2923–2949, 2011.

O Krause, S Birkmann, T Blümchen, A Böhm, M Ebert, U Grözinger, Th Henning, R Hofferbert, A Huber, D Lemke, et al. Cryogenic wheel mechanisms for the mid-infrared instrument (miri) of the james webb space telescope (jwst): detailed design and test results from the qualification program. In *Advanced Optical and Mechanical Technologies in Telescopes and Instrumentation*, volume 7018, pages 758–767. SPIE, 2008.

Konrad Kuijken, David Fisher, and Michael R Merrifield. A search for counter-rotating stars in s0 galaxies. *Monthly Notices of the Royal Astronomical Society*, 283(2):543–550, 1996.

HR Ledo, M Sarzi, Massimo Dotti, S Khochfar, and L Morelli. A census of nuclear stellar discs in early-type galaxies. *Monthly Notices of the Royal Astronomical Society*, 407(2):969–985, 2010.

RVE Lovelace and Tom Chou. Counterrotating accretion disks. *The Astrophysical Journal*, 468(1):L25, 1996.

RVE Lovelace, KP Jore, and MP Haynes. Two-stream instability of counter-rotating galaxies. *The Astrophysical Journal*, 475(1):83, 1997.

Elisabeta Lusso, Michele Fumagalli, Matteo Fossati, Ruari Mackenzie, Richard M Bielby, Fabrizio Arrigoni Battaia, Sebastiano Cantalupo, Ryan Cooke, Stefano Cristiani, Pratika Dayal, et al. The muse ultra deep field (mudf)–i. discovery of a group of $\text{Ly}\alpha$ nebulae associated with a bright $z \simeq 3.23$ quasar pair. *Monthly Notices of the Royal Astronomical Society: Letters*, 485(1):L62–L67, 2019.

Witold Maciejewski. Response of the integrals in the tremaine–weinberg method to multiple pattern speeds: a counter-rotating inner bar in ngc 2950? *Monthly Notices of the Royal Astronomical Society*, 371(1):451–458, 2006.

- Raffaella Anna Marino, Sebastiano Cantalupo, Simon J Lilly, Sofia G Gallego, Lorrie A Straka, Elena Borisova, Gabriele Pezzulli, Roland Bacon, Jarle Brinchmann, C Marcella Carollo, et al. Dark galaxy candidates at redshift 3.5 detected with muse. *The Astrophysical Journal*, 859(1):53, 2018.
- L Morelli, C Halliday, EM Corsini, A Pizzella, D Thomas, RP Saglia, RL Davies, R Bender, M Birkinshaw, and F Bertola. Nuclear stellar discs in low-luminosity elliptical galaxies: Ngc 4458 and 4478. *Monthly Notices of the Royal Astronomical Society*, 354(3):753–762, 2004.
- L Morelli, E Pompei, A Pizzella, J Méndez-Abreu, EM Corsini, L Coccato, RP Saglia, M Sarzi, and F Bertola. Stellar populations of bulges in 14 cluster disc galaxies. *Monthly Notices of the Royal Astronomical Society*, 389(1):341–363, 2008.
- L Morelli, A Pizzella, L Coccato, EM Corsini, E Dalla Bontà, LM Buson, VD Ivanov, I Pagotto, E Pompei, and M Rocco. Kinematic and stellar population properties of the counter-rotating components in the s0 galaxy ngc 1366. *Astronomy & Astrophysics*, 600:A76, 2017.
- Themiya Nanayakkara, Jarle Brinchmann, Leindert Boogaard, Rychard Bouwens, Sebastiano Cantalupo, Anna Feltre, Wolfram Kollatschny, Raffaella Anna Marino, Michael Maseda, Jorryt Matthee, et al. Exploring he ii λ 1640 emission line properties at $z \approx 2$. *Astronomy & Astrophysics*, 624: A89, 2019.
- Terry D Oswalt and Ian S McLean. *Planets, Stars and Stellar Systems: Volume 1: Telescopes and Instrumentation*, volume 298. Springer, 2013.
- Laure Piqueras, Simon Conseil, Martin Shepherd, Roland Bacon, Floriane Leclercq, and Johan Richard. Mpdaf-a python package for the analysis of vlt/muse data. *arXiv preprint arXiv:1710.03554*, 2017.
- A Pizzella, EM Corsini, L Morelli, M Sarzi, C Scarlata, M Stiavelli, and F Bertola. Nuclear stellar disks in spiral galaxies. *The Astrophysical Journal*, 573(1):131, 2002.
- A Pizzella, EM Corsini, JC Vega Beltrán, and F Bertola. Ionized gas and stellar kinematics of seventeen nearby spiral galaxies. *Astronomy & Astrophysics*, 424(2):447–454, 2004.
- H Plana and J Boulesteix. Extended ionized gas in elliptical galaxies. i. multicomponents in ngc 1052 and ngc 7332. *Astronomy and Astrophysics*, 307: 391–402, 1996.

- Michael B Pracy, Scott Croom, Elaine Sadler, Warrick J Couch, Harald Kuntschner, Kenji Bekki, Matt S Owers, Martin Zwaan, James Turner, and Marcel Bergmann. Stellar population gradients and spatially resolved kinematics in luminous post-starburst galaxies. *Monthly Notices of the Royal Astronomical Society*, 432(4):3131–3140, 2013.
- F Prada, CM Gutierrez, RF Peletier, and CD McKeith. A counterrotating bulge in the sb galaxy ngc 7331. *The Astrophysical Journal*, 463(1):L9, 1996.
- I Puerari and D Pfenniger. Ap&ss, 276, 909. doi: 10.1023/A:1017581325673, 2001.
- TD Rawle, Russell J Smith, JR Lucey, and AM Swinbank. Stellar population gradients in early-type cluster galaxies with vimos ifu. *Monthly Notices of the Royal Astronomical Society*, 389(4):1891–1904, 2008.
- Deqing Ren and Jian Ge. An image slicer integral field unit with diffraction-limited performance for three-dimensional imaging spectroscopy. *Publications of the Astronomical Society of the Pacific*, 116(815):46, 2003.
- EH Richardson, JM Fletcher, and WA Grundmann. Image-slicers. In *International Astronomical Union Colloquium*, volume 79, pages 469–492. Cambridge University Press, 1984.
- Hans-Walter R Rix, Robert C Kennicutt Jr, Robert Braun, and Rene AM Walterbos. Placid stars and excited gas in ngc 4826. *The Astrophysical Journal*, 438:155–169, 1995.
- Martin M Roth, Andreas Kelz, Thomas Fechner, Thomas Hahn, Svend-Marian Bauer, Thomas Becker, Petra Böhm, Lise Christensen, Frank Dionies, Jens Paschke, et al. Pmas: The potsdam multi-aperture spectrophotometer. i. design, manufacture, and performance. *Publications of the Astronomical Society of the Pacific*, 117(832):620, 2005.
- Vera C Rubin. Multi-spin galaxies. *The Astronomical Journal*, 108:456–467, 1994.
- Vera C Rubin, JA Graham, and Jeffrey DP Kenney. Cospatial counterrotating stellar disks in the virgo e7/s0 galaxy ngc 4550. *The Astrophysical Journal*, 394:L9–L12, 1992.
- SF Sánchez, RC Kennicutt, A Gil De Paz, G Van de Ven, JM Vílchez, L Wisotzki, CJ Walcher, D Mast, JAL Aguerri, S Albiol-Pérez, et al. Califa, the calar alto legacy integral field area survey-i. survey presentation. *Astronomy & Astrophysics*, 538:A8, 2012.

- Allan Sandage and John Bedke. The carnegie atlas of galaxies. *The Carnegie Atlas of Galaxies. Volumes I*, 638, 1994.
- JA Sellwood and David Merritt. Instabilities of counterrotating stellar disks. *The Astrophysical Journal*, 425:530–550, 1994.
- RG Sharp and Joss Bland-Hawthorn. Three-dimensional integral field observations of 10 galactic winds. i. extended phase (≥ 10 myr) of mass/energy injection before the wind blows. *The Astrophysical Journal*, 711(2):818, 2010.
- Isaac Shlosman, Juhan Frank, and Mitchell C Begelman. Bars within bars: a mechanism for fuelling active galactic nuclei. *Nature*, 338(6210):45–47, 1989.
- O Streicher, PM Weilbacher, R Bacon, and A Jarno. Sky subtraction for the muse data reduction pipeline. In *Astronomical Data Analysis Software and Systems XX*, volume 442, page 257, 2011.
- Aniruddha R Thakar and Barbara S Ryden. Smoothed particle hydrodynamics simulations of counterrotating disk formation in spiral galaxies. *The Astrophysical Journal*, 506(1):93, 1998.
- Aniruddha R Thakar, Barbara S Ryden, Katherine P Jore, and Adrick H Broeils. Ngc 4138: a case study in counterrotating disk formation. *The Astrophysical Journal*, 479(2):702, 1997.
- HC Van de Hulst, E Raimond, and H Van Woerden. Rotation and density distribution of the andromeda nebula derived from observations of the 21-cm line. *Bulletin of the Astronomical Institutes of the Netherlands*, 14:1, 1957.
- Roeland P Van Der Marel and Marijn Franx. A new method for the identification of non-gaussian line profiles in elliptical galaxies. *The Astrophysical Journal*, 407:525–539, 1993.
- A Vazdekis, E Ricciardelli, AJ Cenarro, JG Rivero-González, LA Díaz-García, and J Falcón-Barroso. Miuscat: extended miles spectral coverage–i. stellar population synthesis models. *Monthly Notices of the Royal Astronomical Society*, 424(1):157–171, 2012.
- D Vergani, A Pizzella, EM Corsini, W Van Driel, LM Buson, R-J Dettmar, and F Bertola. Ngc 5719/13: interacting spirals forming a counter-rotating stellar disc. *Astronomy & Astrophysics*, 463(3):883–892, 2007.
- RAM Walterbos, R Braun, and RC Kennicutt Jr. The optical morphology of the kinematically peculiar galaxy ngc 4826. *The Astronomical Journal*, 107:184–194, 1994.

Peter M Weilbacher, Ole Streicher, Tanya Urrutia, Arlette Pécontal-Rousset, Aurélien Jarno, and Roland Bacon. The muse data reduction pipeline: status after preliminary acceptance europe. *arXiv preprint arXiv:1507.00034*, 2015.

Peter M Weilbacher, Ole Streicher, and Ralf Palsa. Muse-drp: Muse data reduction pipeline. *Astrophysics Source Code Library*, pages ascl–1610, 2016.

Hervé Wozniak and Daniel Pfenniger. ” rotation curves” in self-consistent models of barred galaxies. *Astronomy and Astrophysics*, 317:14–24, 1997.